An optimized, parameter-free PML-FEM for wave scattering problems in the ocean and coastal environment

A. E. Karperaki[a], T. K. Papathanasiou[b] and K. A. Belibassakis[a] (*)

[a]School of Naval Architecture and Marine Engineering
National Technical University of Athens, Zografos 15773, Athens, Greece
[b]Department of Civil and Environmental Engineering,
Brunel University London, Uxbridge UB8 3PH, UK

ABSTRACT

Water-wave propagation in nearshore regions and hydroacoustic scattering problems, in the presence of structures, are fundamental to ocean and coastal engineering. Efficient modelling of these phenomena can be achieved using the Helmholtz equation with spatially varying coefficients to which mild-slope models are reducible. Despite the relatively simple forms of these models, geometric and medium inhomogeneities and inclusions, yield complex wavefield solutions that can only be numerically approximated. However, the numerical treatment of such problems in infinite domains requires the truncation of the computational region. In this work, an optimal, parameter-free Perfectly Matched Layer (PML) model is implemented in a Finite Element scheme. The fundamental similarities between the governing equations for steady-state water wave and hydroacoustic scattering problems allow for a joint analysis of the proposed PML-FEM solution strategy. Excellent convergence characteristics are verified through comparisons against benchmark solutions. Water-wave propagation solutions for an uneven seabed featuring an elliptic shoal are compared with available experimental data. Also, wave diffraction by vertical cylinders in regions of variable bathymetry, and scattering by an elliptically shaped body in the ocean-acoustic waveguide, are studied. The proposed numerical scheme is found to be an efficient means to tackle challenging wave-seabed-body interaction problems in large spatial domains.

Keywords: wave-seabed-body interaction, multiple scattering, inhomogeneous media, PML-FEM

1 Introduction

The accurate prediction of wave fields in nearshore and coastal areas is crucial for several applications, including the design and safe operation of marine structures and harbours, as well as the stability of the coastal zone. In many cases, ranging from the design of pile breakwaters to offshore wind farms, the interaction of free-surface gravity waves with uneven bottom topography and surface-piercing obstacles, like vertical cylinder arrays, is of great significance for engineering studies; see, e.g., Guo et al. (2017) and Ruiz et al. (2017). To facilitate the analysis in variable bathymetry regions the assumption of moderate bottom slopes is usually adopted, and hence the wave conditions are determined by means of reduced refraction-diffraction, mild-slope type models; see, e.g., Mei (1994) and Dingemans (1997). Such models, typically involving only the horizontal spatial variables, allow for the study of water wave diffraction in the presence of obstacles, while accounting for refraction effects due to a mildly sloping bottom. In the work of Booij (1983) it is shown that the applicability of the classical mild-slope model proposed by Berkhoff (1972, 1982) is limited to bottom slopes up to 1:3. Enhancements of the classical model, in order to account for stronger bottom variations, led to modified versions presented by various authors, e.g., Radder and Dingemans (1985), Massel (1993), Chamberlain and Porter (1995). Additional effects concerning dissipation due to bottom friction and wave breaking, as well as wave-current interaction, have also been presented in the works of , Liu (1983) and Kirby (1984); see also Belibassakis et al. (2011, 2014). Notably, the elliptic mild-slope models are reduced to the Helmholtz equation with variable coefficients (see, e.g., Mei 1994). The above fact underlines the similarity between the combined refraction-diffraction problem for water-waves on the horizontal plane and hydroacoustic wave propagation and scattering in the inhomogeneous ocean and coastal waveguides that is also modelled by the Helmholtz equation (Brekhovskikh and Lysanov, 2003; Jensen et al., 2011). These similarities allow for the development of common methods and techniques regarding their numerical treatment; see also Chai et al. (2016).

Apart from being governed by the same equation, the above problems also share the characteristic of being inherently formulated in unbounded or partially unbounded domains. This class of problems is further complicated by the fact that the physical properties of the medium (the propagation speed or the index of refraction) are variable at infinity, as approached from different directions. In this case, the far-field wave pattern is not known a priori, and a standard radiation condition (e.g., Sommerfeld condition) is not available. The truncation of the unbounded domain, in conjunction with efficient implementation of closure conditions at the truncated boundary, is hence required. To this purpose, a number of strategies have been developed in the literature, across disciplines. Absorbing Boundary Conditions (ABCs), approximate DtN operators, infinite elements and boundary element methods have been widely used to truncate problems that are naturally defined in infinite domains; see, e.g., Givoli (1991, 1992). ABC techniques are concerned with the development of radiation condition variants that are able to model the effects of the exterior domain on the open boundary. Since the artificial boundary conditions are constructed to approximately minimize spurious reflections, important issues concerning the order of accuracy and its computational cost rise. Moreover, knowledge of the solution characteristics in the far-field is frequently required for an effective implementation. Additionally, the efficiency of lower order ABCs increases as the open boundary is positioned further away from the scatterer, which makes accuracy a tradeoff for computational labour. On the other hand, the employment of the above models

involving higher-order derivatives can prove computationally tedious. Higher-order ABCs, able to achieve enhanced accuracy without excessive computational cost, are reviewed in Givoli (2004). A commonly cited advantage of ABCs is the ease of their implementation in FE solvers, since the produced sparse matrices are preferable to the dense matrices produced by non-local DtN strategies.

Opposed to ABCs and DtN methods, perfectly-matched layer (PML) models do not introduce approximate conditions at the external fictitious boundary but a layer with damping qualities, enclosing the computational domain. The complex medium is constructed in such a way that the solution at the interface between the absorber and the domain of interest are perfectly matched, thus suppressing spurious reflections. The classical PML model by Berenger (1994) imposed matching conditions between the incident wavefield and the attenuated solutions for the time-dependent Maxwell equations. The initial split field approach is equivalent to complex coordinate stretching as indicated in the works of Rappaport (1995) and others. The rate of solution attenuation within the layer is dictated by the use of a suitable absorbing function; see Abarbanel and Gottlieb (1997), Turkel and Yefet (1998). A unique and rather desirable quality of PML-based methods over most boundary termination techniques is that their effectiveness is independent of the angle of incidence to the fictitious boundary as well as of the wave frequency. Since the original application by Berenger (1994) to the solution of the Maxwell equations, PML models have been successfully implemented in the treatment of several problems which are naturally defined in infinite domains, such as acoustic scattering (e.g., Qi and Geers 1998), elasticity (e.g., Harari and Albocher 2006) and water waves (e.g., Belibassakis et al., 2001; Navon et al., 2004; Modesto et al. 2015).

The exponential convergence of the PML to the exact solution of the reduced wave equation as the layer thickness tends to infinity is shown by Lassas and Somersalo (1998). However, the numerical treatment requires a finite layer, thus introducing error due to reflection at the exterior, termination boundary. Even so, the dissipative properties of a finite PML are ensured by allowing for sufficient layer thickness or by the employment of an appropriate absorbing function. Such function should minimize the reflection at the outer boundary to eliminate contamination of the numerical solution. However, in computational applications numerical reflections do rise due to discretization. Collino and Monk (1998a) suggested that the numerical error is effectively contained by optimizing the absorbing function. In the same work, it was shown that the choice of the absorbing function and the discretization within the layer affects the reflection coefficient in a non-trivial manner, raising the question of an optimal or parameter-dependent PML at the discretized level. The parameters for optimization are the employed mesh, the layer thickness and the functional form of the absorbing function. Regarding the latter, constant and polynomial functions of a varying degree have been introduced (Berenger, 1994; Collino and Monk, 1998b; Singer and Turkel, 2004). Recently, a novel PML formulation was proposed by Bermudez et al. (2007) featuring an unbounded absorbing function; see also Bermudez et al. (2010) and references therein. It is shown that the latter singular PML model is able to recover the exact solution for the unbounded scalar Helmholtz equation. The formulation retains the desirable qualities of classical PML approaches without the need to further optimize the parameters of the absorbing function according to the employed mesh and problem data. Hence, by introducing an unbounded absorbing

function, PML thickness is the only parameter to be optimized as noted by Cimpeanu et al. (2015), who also studied the correlation between numerical error and employed layer thickness of the optimal PML (Bermudez et al., 2007). Most interestingly they note the existence of an optimal normalised thickness range where the numerical error remains insensitive to change, suggesting that within this range the model is rendered parameter-free. Notably, the suggested thickness ranges are very small reducing the computational cost and making the method further appealing. Finally, in the work of Rabinovich et al. (2010) a comprehensive comparison between ABCs and PML models is carried out, showing that the effectiveness of the PML with an unbounded absorbing function is similar to that of higher-order ABC. While the former is insensitive to the employed discretization and requires no-tuning, higher-order ABCs remain considerably more complex in implementation than the singular PML, which is straightforward to incorporate in a FEM-based solver.

In the present work, a PML featuring an unbounded absorbing function (Bermudez et al., 2007, Cimpeanu et al., 2015), for water-wave and hydroacoustic propagation and scattering problems is investigated. These problems are governed by the Modified Mild Slope and the Helmholtz equations, with variable coefficients respectively. The optimal, parameter-free PML model is implemented in a FE strategy for the numerical solution of the wave-seabed-body interaction problems. In Sec. 2, the mathematical formulation is presented for water wave propagation on the horizontal plane and for acoustic scattering in a vertical infinite strip modelling the ocean-coastal waveguide. Subsequently, the weak forms of the truncated problems are provided in Sec. 3 following a unified presentation. Next, in Sec. 4, the implementation issues of the PML-FEM are discussed. Moreover, the error of the present method against benchmark analytical solutions, which are reviewed in the Appendix, is calculated and results concerning the convergence characteristics are shown, demonstrating a very good performance. In Sec.5 the present method is validated against experimental data in the case of water-wave propagation over an uneven seabed featuring an elliptic shoal. Finally, additional numerical examples involving diffraction by vertical cylinders, which are assumed founded in variable bathymetry regions, and acoustic scattering by a generally shaped body in the ocean waveguide, are studied.

2 Scattering problems in inhomogeneous regions

2.1 Linear water wave propagation and scattering

In the present section, a unified presentation is followed for problems of water-wave propagation in nearshore regions, including the case of wave interaction with bottom founded obstacles, and hydroacoustic propagation in the complex ocean waveguide in the presence of acoustic scatterers. Small amplitude, steady state water waves in coastal regions and hydroacoustic waves can be modelled using elliptic partial differential equations. In particular, both problems are governed by the Helmholtz equation with spatially varying coefficients, in conjunction with appropriate conditions simulating the effects of boundaries. The numerical solution of this type of problems is characterized by increased complexity due to variations of the parameters and the presence of scatterers. Additionally, as the frequency of the waves increases, accurate numerical solutions require significant computational effort.

Initially, we consider the case of harmonic water-wave propagation in variable bathymetry regions. Assuming only a mildly sloping seabed, the Mild Slope Equation (MSE) is a classical model, obtained by integration over the water depth leading to a dimensionality

Published in Ocean Engineering - Volume 179, 1 May 2019, Pages 307-324

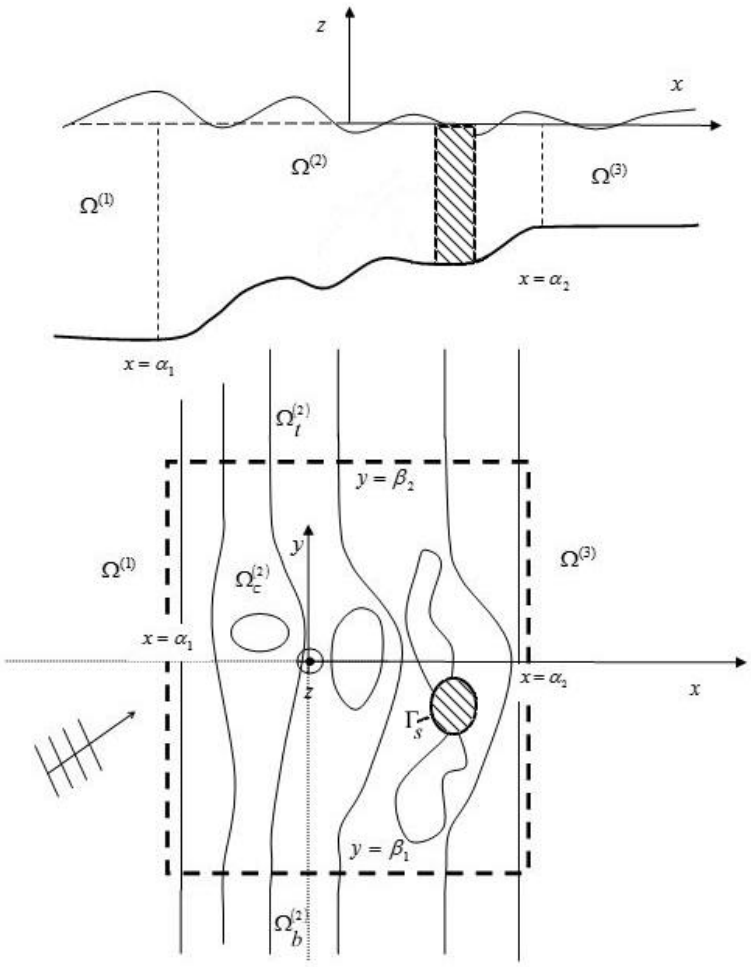

Figure 1. Water wave propagation over a general, mildly sloped bathymetry featuring localised shoals and the presence of a bottom-founded structure (scatterer extending over the water column shown by the shaded area).

reduction of the 3D water wave problem; see e.g., Dingemans (1997). An enhanced version of the above model is the Modified Mild Slope equation (MMS), presented by Massel (1993) and Chamberlain and Porter (1995). This model is able to account for higher-order effects involving the gradients of the depth function. The latter elliptic model, supplemented by appropriate conditions at fixed boundaries and the description of the incident wave field and/or radiation conditions at open boundaries, is commonly applied to study wave transformations in coastal regions and in harbour design. In this case, the considered marine environment is composed of a layer of inviscid and irrotational fluid bounded above by a free surface and below by a rigid, impermeable bottom. A Cartesian coordinate system $\mathbf{x}(x, y, z)$ is introduced, with the origin placed on the mean water level, and the z axis pointing upwards; see Fig. 1. The examined domain $\Omega \subset \mathbb{R}^2$ can be divided into three regions, the region of wavefield incidence $\Omega^{(1)}$, characterized by a constant bathymetry h_1, the region of transmission $\Omega^{(3)}$ with a constant bathymetry h_3 and region $\Omega^{(2)}$ located between the two and featuring a variable seabed. Region $\Omega^{(2)}$ is further

decomposed into subregions $\Omega_t^{(2)}, \Omega_b^{(2)}$ and $\Omega_c^{(2)}$. Sub-regions $\Omega_t^{(2)}\left(y > \beta_2\right)$ and $\Omega_b^{(2)}\left(y < \beta_1\right)$ feature the parallel contour bathymetric profile denoted by $h_i(x)$, while the bathymetry in $\Omega_c^{(2)}$ includes the depth inhomogeneity $h_d(x,y)$, resembling a shoaling region, acting as a localised scatterer formation superimposed over the parallel contour surface. In this work, depth functions $h_i(x)$ and $h_d(x,y)$ are assumed to be smooth functions, with continuous first and piecewise continuous second derivatives. The projection of the submerged, localized scatterer boundary on the plane of propagation is denoted as Γ_s. It is understood that the depth inhomogeneity imposes a disturbance over the parallel contour morphology of the seabed and the total depth function in the present analysis is decomposed as, $h_2 = h(x,y) = h_i(x) + h_d(x,y)$. Similarly, the total wavefield solution is decomposed into an unknown incident field, carrying the imposed wave transformations due to the presence of the parallel contour bathymetry $h_i(x)$ and an unknown, diffracted field attributed to the presence of the localized scatterer corresponding to the depth function perturbation $h_d(x,y)$. Hence, the total wave potential solution on the horizontal plane is the sum $\varphi_i + \varphi_d$.

The MMS equation is employed for each of the reduced problems on φ_i and φ_d. For an obliquely incident wave, the solution $\varphi_i\left(x,y\right)$ is periodic along the y direction, and can be expressed as $\varphi_i\left(x,y\right) = e^{ik_y y}\phi_i\left(x\right)$, with $k_y = k_0^{(1)}\sin\theta_I$, where $k_0^{(1)}$ is the wavenumber at the region of incidence $\Omega^{(1)}$, θ_I is the angle of wave incidence with respect to the parallel contours of the seabed, and $i = \sqrt{-1}$. Thus, the propagating-refracted-diffracted wavefield $\phi_i\left(x\right)$ over the parallel contour bathymetric profile $h_i\left(x\right)$ satisfies the following one-dimensional (x-dependent) MMS equation:

$$\frac{\partial}{\partial x}\left(cc_g\frac{\partial\phi_i\left(x\right)}{\partial x}\right) + cc_g\left[\left(k_0{}^2 + \psi_0\right) - k_y^2\right]\phi_i\left(x\right) = 0, \quad x \in \Omega^{(2)}. \tag{1}$$

In Eq. (1) $c\left(x\right) = \omega/k_0\left(x\right)$ is the phase velocity and $c_g\left(x\right) = \partial\omega/\partial k$ is the corresponding group velocity, where the angular frequency of the monochromatic incident wave is denoted by ω and the local wavenumber by $k_0\left(x\right)$. The latter is obtained from the dispersion relation, $\omega^2 = k_0\left(x\right)g\tanh\left[k_0\left(x\right)h_i\left(x\right)\right]$, with g being the acceleration of gravity. The function ψ_0 involves terms of bottom slope and curvature of the depth function $h_i(x)$ and can be found in Massel (1993, Eq.34); see also Miles and Chamberlain (1998). Equation (1) is supplemented by appropriate incident and outgoing boundary conditions at $x = a_1$ and $x = a_2$, respectively.

The diffraction problem on $\varphi_d\left(x,y\right)$, over the real bathymetry $h\left(x,y\right)$ behaves like a radiating solution as $\sqrt{x^2+y^2} \to \infty$, and satisfies the MMSE on the horizontal plane as

$$\nabla\left(cc_g\nabla\varphi_d\right) + cc_g\left(k^2 + \psi\right)\varphi_d = f, \quad x, y \in \Omega_c^{(2)}, \tag{2}$$

where ∇ is the 2D horizontal gradient operator. Again $k = k\left(x,y\right)$ is the local wavenumber obtained as the root of the dispersion relation formulated at the local depth $\omega^2 = k\left(x,y\right)g\tanh\left[k\left(x,y\right)h\left(x,y\right)\right]$, and ψ is similarly defined in terms of bottom slope

and curvature of the depth function $h(x,y)$. The forcing term $f(x,y)$ in the right-hand side of Eq. (2) is obtained from the solution of the propagating wavefield φ_i, as follows $f=-\left[\nabla\left(cc_g\nabla\varphi_i\right)+cc_g\left(k^2+\psi\right)\varphi_i\right]$, and has support on the projection Γ_s of the depth inhomogeneity $h_d(x,y)$. It can be easily seen that by the substitutions $\Phi_i=\sqrt{cc_g}\phi_i$ and $\Phi_d=\sqrt{cc_g}\varphi_d$, both Eqs. (1) and (2) reduce to the Helmholtz equation with a horizontally varying coefficient κ corresponding to an effective wavenumber; see, e.g., Radder, (1979) Mei (1994). Focusing on the diffraction problem, Eq. (2) takes the form,

$$\nabla^2\Phi_d(x,y)+\kappa^2\Phi_d(x,y)=\frac{f(x,y)}{\sqrt{cc_g}},\ x,y\in\Omega_c^{(2)},\ \text{with}\ \kappa^2=\left(k^2+\psi\right)-\frac{\nabla^2\sqrt{cc_g}}{\sqrt{cc_g}}. \tag{3}$$

As mentioned above the total solution for the refracted-diffracted wavefield in the presented formulation is derived by the superposition of the incident-refracted wavefield Φ_i and the diffracted wavefield Φ_d.

Next, the case of wavefield diffraction over a single or multiple scatterers, which are assumed to be vertical cylinder(s) of general cross section, extending over the whole length of the water column (from the seabed to the free surface) is considered. These localized scatterers, denoted as S_i, lay in the interior of the computational domain $\Omega'=\Omega\setminus\bar{S}$, where $S=\bigcup S_i$ is the union of the disjoint inclusions S_i with smooth boundaries Γ_{si}, so that the solid boundary is given as $\Gamma_s=\bigcup\Gamma_{si}$ and $\bar{S}=S\bigcup\Gamma_s$. More specifically, following the same domain decomposition, the inclusions are assumed to be contained in $\Omega_c^{(2)}$. The harmonic water wave diffraction problem over the parallel contour bathymetry $h_2=h_i(x,y)$ in the presence of the scatterers S_i, is again governed by the MMS model in the horizontal plane which is now given by,

$$\nabla^2\Phi_d(x,y)+\kappa^2\Phi_d(x,y)=0,\quad x,y\in\Omega_c^{(2)}\setminus\bar{S} \tag{4}$$

supplemented by a suitable boundary condition on the body surfaces,

$$\alpha\frac{\partial\Phi_d}{\partial n}+\beta\Phi_d=-\left(\alpha\frac{\partial\Phi_i}{\partial n}+\beta\Phi_i\right)\ \text{on}\ \Gamma_s \tag{5}$$

where α and β are constants in general, depending on the body properties. In the case of rigid structures the selection $\alpha=1,\ \beta=0$ reduces to the standard Neumann condition. The known Cauchy incident data on Γ_s (in the right-hand side of Eq. 5) are provided again by the solution of the incident-refracted wavefield problem Φ_i, over the parallel contour bathymetry $h_i(x)$ in the absence of the inclusions as in the previous case. The key difference between the above two problems, defined by Eq. (3) and Eqs (4), (5), is that in the former case, wave diffraction is caused by the assumed depth inhomogeneity $h_d(x,y)$, superimposed over the variable bathymetry, while in the latter case wave scattering takes place because of the presence of the surface piercing bodies in the region of interest. Obviously, the present method is capable to treat the combined effects.

2.2 Hydroacoustic wave propagation and scattering in the ocean waveguide

In the sequel, the problem of hydroacoustic wave propagation in the inhomogeneous ocean waveguide is considered. Propagation and scattering problems in underwater acoustics, and more specifically in range-dependent domains relevant to coastal applications, are frequently formulated by using a point source (see e.g. Jensen et al., 2011) for field excitation.

However, as frequency increases, the problem becomes computationally demanding, and thus, for many practical problems, as well as for inter-model comparisons, it is useful to work with a line source in plane geometry; see Fig. 2. Assuming constant medium

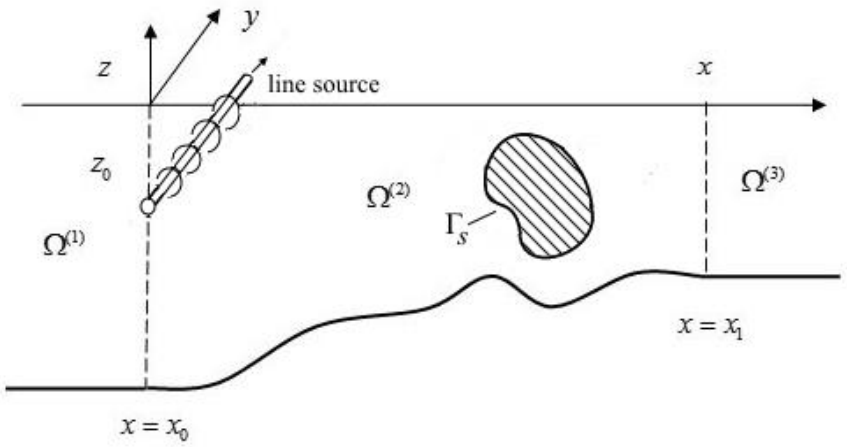

Figure 2. Hydroacoustic waves emitted from a line source at depth, z_0 propagating in the vertical plane in a range dependent environment and scattered by a submerged body (localized scatterer) with boundary Γ_s.

properties along the transverse y direction, the line source can be visualised as a distribution of monopole sources along the y axis. In this case, underwater acoustic wave propagation is governed by the Helmholtz equation on the vertical plane, while the acoustic waveguide is formed by the free upper surface and seabed boundaries. The domain of interest is thus an inhomogeneous strip, denoted as $\Omega = \Omega^{(1)} \bigcup \Omega^{(2)} \bigcup \Omega^{(3)}$, which is again decomposed into three parts, the near and far field subdomains $\Omega^{(1)}$ and $\Omega^{(3)}$ respectively, and the middle subregion $\Omega^{(2)}$. The strip is terminated at the free surface at $z = 0$, and at the seabed at $z = -h(x)$, which for simplicity is assumed to be acoustically hard in this work, where $h(x)$ is again the depth function.

The body(ies) S_i, with smooth boundary Γ_{si}, are representing acoustic scatterers similar to the previous sub-section formulation and are contained in $\Omega^{(2)}$. Again it holds that $S = \bigcup S_i$, $\Gamma_s = \bigcup \Gamma_{si}$ and $\bar{S} = S \bigcup \Gamma_s$. In the lateral subregions, the seabed is considered to be flat with the depth function assuming the constant values h_1 and h_3 in $\Omega^{(1)}$ and $\Omega^{(3)}$ respectively. Additionally, these areas are considered to be range independent, hence the acoustic medium properties are assumed to exhibit only vertical variation. In the considered case, the mathematical problem of hydroacoustic propagation in a range-dependent waveguide, excited by a line source, is described as,

$$\frac{\partial^2 \Phi}{\partial x^2} + \frac{\partial^2 \Phi}{\partial z^2} + k^2(x,z)\Phi = -\delta(x - x_0)\delta(z - z_0),\ x, z \in \Omega \setminus \bar{S} \quad , \tag{6}$$

where Φ denotes the acoustic wavefield in the waveguide. The acoustic wavenumber is denoted as $k(x,z)=\omega/c(x,z)$, where $c(x,z)$ is the speed of sound propagation in the medium characterised by a variable index of refraction.
The problem is supplemented at the upper and bottom boundaries by the following conditions, respectively,

$$\Phi=0\text{, on } z=0 \qquad \text{and} \qquad \partial\Phi/\partial n=0 \text{ on } z=-h(x). \tag{7a,b}$$

In the present work, the seabed is modelled as an acoustically hard boundary, however, extension to treat a multilayered bottom is possible; see, e.g., Jensen et al. (2011). The total wavefield can be once again split into a solution that carries the field transformations due to the variable index of refraction of the medium, in the absence of the finite body(ies), and a scattered solution due to the presence of the body(ies) in the waveguide. The total wavefield is decomposed to the incident and scattered acoustic wavefields as, $\Phi_t=\Phi_i+\Phi_s$. The former can be calculated by several methods, as e.g., the coupled-mode method (see, e.g., Belibassakis et al., 2014 and references cited therein) where the solution is represented by

$$\Phi_i(x,z)=\sum_{n=0}^{\infty}\varphi_n(x)\tilde{Z}_n(z;x), \tag{8a}$$

while $\varphi_n(x)$ are the modal amplitudes and $\tilde{Z}_n(z)=Z_n(z;x)/\|Z_n\|$ are the normalised local vertical eigenmodes satisfying the boundary conditions (7). In the case of a range independent environment over a flat rigid bottom with constant depth *h*, the above expansion reduces to the corresponding normal-mode series (see also Jensen et al., 2011)

$$\Phi_i(x,z)=2\sum_{n=0}^{\infty}\tilde{Z}_n(z)\tilde{Z}_n(z_0)\frac{\exp\left(ik_{xn}|x-x_0|\right)}{k_{xn}}, \tag{8b}$$

where $Z_n(z)=\sin(k_{zn}z)$, $k_{zn}=(n-0.5)\pi/h$, and $k_{xn}=\sqrt{k^2-k_{zn}^2}$ are the horizontal wavenumbers. Additional details are provided in the Appendix. The location of the line source is denoted by (x_0,z_0). Consequently, the scattering problem in the waveguide containing the localised scatterer(s) S_i is formulated as,

$$\frac{\partial^2\Phi_s}{\partial x^2}+\frac{\partial^2\Phi_s}{\partial z^2}+k^2(x,z)\Phi_s=0\ ,\quad x,z\in\Omega\setminus\bar{S} \tag{9}$$

where $k(x,z)$ is spatially varying acoustic wavenumber. Eq. (9) is supplemented by the following boundary condition

$$\alpha\frac{\partial\Phi_s}{\partial n}+\beta\Phi_s=-\left(\alpha\frac{\partial\Phi_i}{\partial n}+\beta\Phi_i\right)\ \text{, on } \Gamma_s. \tag{10}$$

Again, coefficients α and β are in general dependent on the frequency, and are determined by the scatterer properties, with $\alpha=1$ and $\beta=0$ corresponding to an acoustically hard surface, and $\alpha=0$ and $\beta=1$ to an acoustically soft body. The Cauchy data on Γ_s are derived by the representation of the incident wavefield Φ_i (as in Eqs. 8).

Similarities between the examined refraction-diffraction problems for water-wave propagation on the horizontal plane, Eqs. (3) and (4-5), and hydroacoustic scattering on the vertical plane, Eqs. (9-10), are profound. In both cases the resulting Helmholtz-type problems with varying coefficients, defined in unbounded domains and supplemented with appropriate conditions on the enclosed scatterer boundaries, allow for the development and implementation of similar computational methods. Standard methods for the numerical treatment of the Helmholtz equation with spatially variable coefficients are Finite Difference and Finite Element schemes (see Oliveira and Anastasiou, 1998; Panchang et al, 1991; Belibassakis et al., 2001). A major challenge in devising a numerical scheme for problems in (partially of totally) unbounded domains, governed by PDEs with variable coefficients, is to ensure energy absorption at the open boundaries with minimum backscattering. An extended discussion of appropriate conditions for the elliptic mild-slope equation can be found in the work of Oliveira (2004). In this direction, Collino and Monk (1998) studied the PML model by Berenger (1994) as a closure condition for the Helmholtz equation in acoustic and electromagnetic propagation problems, while Modesto et al. (2015, 2016) employed the same model in conjunction with the MSE for the study of harbour agitation. The effectiveness of the above PML is strongly dependent on the layer parameters (thickness, absorbing function form). In the next section the parameter-free PML model by Bermudez et al. (2007) is applied, in conjunction with the FE method, for the optimal solution of the presented diffraction/scattering problems in the coastal environment.

3 Implementation of the PML-FE strategy

3.1 Domain truncation with a PML

The diffraction problems presented in Sec. 2, in the framework of linear water wave and hydroacoustic wave propagation, are examined in the 2D horizontal space and the 2D vertical strip, respectively. In this section, a unified approach in the truncation of the physical domains and the application of a PML is pursued first. Subsequently, the weak forms of the truncated problems will be examined from the convergence and accuracy point of view.

The water-wave diffraction problem, governed by the Helmholtz equation with variable coefficients (see Eqs. 3, 4 and 5) is reformulated in a truncated domain by means of a PML of finite thickness θ. The introduced 2D layer is confined in the region $\Omega_{\text{pml}} = [-\mathrm{X}_1 - \theta, \mathrm{X}_1 + \theta] \times [-\mathrm{X}_2 - \theta, \mathrm{X}_2 + \theta] \setminus [-\mathrm{X}_1, \mathrm{X}_1] \times [-\mathrm{X}_2, \mathrm{X}_2]$ extending in both horizontal directions, denoted here as $\mathbf{x} = (x_1, x_2)$ for ease in presentation. The inner rectangle, $\Omega_{\text{r}} = [-\mathrm{X}_1, \mathrm{X}_1] \times [-\mathrm{X}_2, \mathrm{X}_2]$ enclosing the scatterer(s), constitutes the region of computational interest (see Fig. 3a). The fictitious outer termination boundary is denoted by Γ_{E} while the interface between the computational region and the PML is Γ_{I}. The outward normal vector on the interface is denoted by $\mathbf{v} = (v_1, v_2)$. The surface of the scatterer is again denoted by Γ_{S} and $\mathbf{n} = (n_1, n_2)$ is the outward normal vector on the inclusion(s) boundary.

The Cartesian PML for the hydroacoustic scattering problem, governed by the Helmholtz equation in the infinite strip is similarly defined. The computational waveguide is confined in the bounded strip $\Omega_s : [-\mathrm{X}_1, \mathrm{X}_1] \times [-h/2, h/2]$ enclosing the scatterer with the PML $\Omega_{\text{pml}}^{(1)} : [-\mathrm{X}_1 - \theta, -\mathrm{X}_1] \times [-h/2, h/2]$, $\Omega_{\text{pml}}^{(2)} : [\mathrm{X}_1, \mathrm{X}_1 + \theta] \times [-h/2, h/2]$ and positioned at each side of the strip (see Fig. 3b). The lateral interface boundaries between the PML

subregions and the truncated strip are denoted as $\Gamma_I = \Gamma_I^{(1)} \cup \Gamma_I^{(2)}$ while the external termination boundaries are given as $\Gamma_E = \Gamma_E^{(1)} \cup \Gamma_E^{(2)}$. Similarly, the upper and lower boundaries of the strip are denoted as $\Gamma_B = \Gamma_B^{(1)} \cup \Gamma_B^{(2)}$.

As already mentioned, in PML-based methods the solution matching in the absorber interface can be achieved by its complex coordinate stretching in the layer region (Collino and Monk, 1998a; Bermudez et al., 2007). The notion behind the latter approach is the analytic continuation of a real function into the complex plane. In the physical, unbounded domain, the analytically continuous, wave-like solutions are stretched in a complex contour which allows for oscillating solutions to be turned into decaying waves outside the region of computational interest.

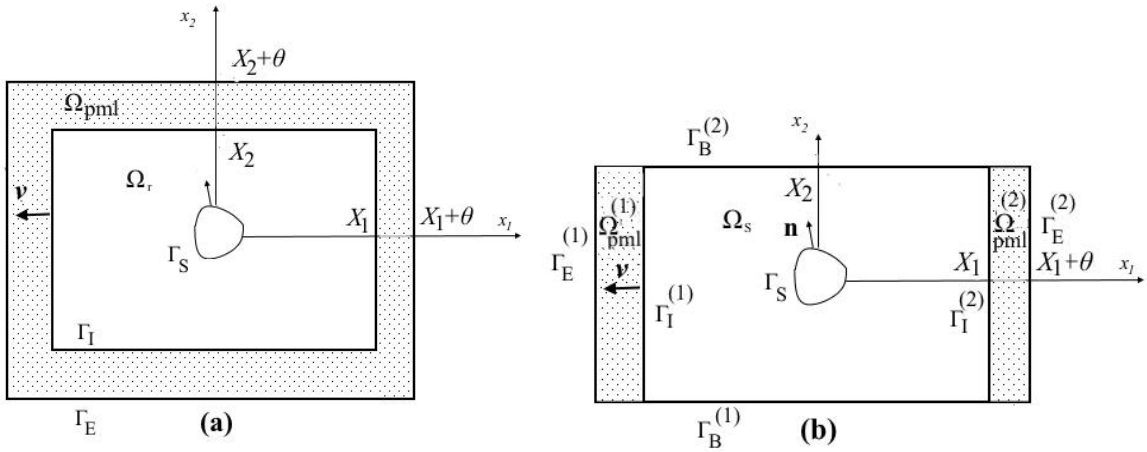

Figure 3. Configuration of the computational domain including the PML regions for the cases of (a) the MMS on the horizontal plane (left). (b) the Helmholtz equation in the acoustic waveguide on the vertical plane (right).

The following complex coordinate transformation is introduced, supported in both vertical and horizontal PML regions,

$$\tilde{x}_i = X_i + \int_{|X_i|}^{|x_i|} \gamma_i(s)\, ds,\ \mathbf{x} \in \Omega_{\text{pml}} \ \text{ for } i = 1,2 \quad , \tag{11}$$

with $\gamma_i(x_i)$ being appropriate complex functions defined along the directions x_1 and x_2 accordingly, while the tilde denotes the complex contour coordinate.

The absorbing functions $\gamma_i(x)$ are of the general form,

$$\gamma_i(x_i) = \begin{cases} 1 & , \mathbf{x} \in \Omega_* \\ 1 + i\dfrac{\sigma_i(x_i)}{k} & , \mathbf{x} \in \Omega_{\text{pml}} \end{cases} , \tag{12}$$

where Ω_* refers to either Ω_r or Ω_s. Furthermore it is denoted that $\tilde{\Omega} = \Omega_* \cup \Omega_{\text{pml}}$.

By reducing the transformation functions to unity, the solution remains unchanged in the domain of interest, while the general complex form assumed inside the layer is associated with the desirable attenuation characteristics in the PML region. The rate of wave damping

is determined by the form of the employed functions $\sigma_i(x_i), i=1,2$ acting on the vertical and horizontal layers. The choice of $\sigma_i(x_i)$ profiles is independent of the present analysis and will be addressed in a following subsection. It is evident however that in order to ensure decaying solutions within the PML, non-negative functions must be considered. After performing the following change of variables in the layer,

$$\frac{\partial}{\partial \tilde{x}_i} \rightarrow \frac{1}{\gamma_i(x_i)} \frac{\partial}{\partial x_i} \quad \text{for} \quad i=1,2 \quad , \tag{13}$$

the governing equation is written in compact form as

$$\nabla \cdot (\boldsymbol{\gamma} \nabla \varphi) + k^2 |\boldsymbol{\gamma}_+| \varphi = 0 \quad \text{for} \quad \mathbf{x} \in \tilde{\Omega} , \tag{14}$$

by means of the matrix

$$\boldsymbol{\gamma} = \boldsymbol{\gamma}_+ \boldsymbol{\gamma}_- = \begin{bmatrix} \gamma_2^{\mu} & 0 \\ 0 & \gamma_1^{\lambda} \end{bmatrix} \begin{bmatrix} \gamma_1^{-\lambda} & 0 \\ 0 & \gamma_2^{-\mu} \end{bmatrix} = \begin{bmatrix} \gamma_2^{\mu} \gamma_1^{-\lambda} & 0 \\ 0 & \gamma_1^{\lambda} \gamma_2^{-\mu} \end{bmatrix}, \tag{15}$$

where,

$\lambda = 1,\ \mu = 1$, for the 2D horizontal space,

$\lambda = 1,\ \mu = 0$, for the infinite strip spanning along the x_1 axis and

$\lambda = 0,\ \mu = 1$, for an infinite strip spanning along the x_2 axis.

Equation (15) is derived by imposing the coordinate transformation described in Eq. (13) in the field equation. Outside the layer, $\boldsymbol{\gamma}$ reduces to the unit matrix, thus leaving the Helmholtz operator unchanged in Ω_*. The constants λ, μ are used for the compact presentation of both problems of interest. When defined in the infinite strip, Eq. (14) needs to be supplemented by appropriate conditions at the upper and lower boundaries. As seen in Sec. 2, in hydroacoustics these conditions are described by Eqs. (7)

The mixed-type condition on the scatterer surface, contained in the computational region, is again valid,

$$\alpha \frac{\partial \varphi}{\partial n} + \beta \varphi = -\left(\alpha \frac{\partial \Phi_i}{\partial n} + \beta \Phi_i \right) \text{ on } \Gamma_S \tag{16}$$

where Φ_i denotes the incident wavefield and the right-hand side of the above equation is linear combination of the known incident data on the surface of the scatterer(s). On the internal boundary between the PML and the computational domain, the continuity requirement poses the following conditions on the function φ and its normal derivative on the boundary,

$$\varphi_- = \varphi_+ \ , \text{and} \tag{17a}$$

$$\frac{\partial \varphi_-}{\partial \nu_1} + \frac{\partial \varphi_-}{\partial \nu_2} = \frac{1}{\gamma_1} \frac{\partial \varphi_+}{\partial \nu_1} + \frac{1}{\gamma_2} \frac{\partial \varphi_+}{\partial \nu_2} \quad \text{on } \Gamma_I \ . \tag{17b}$$

These conditions are satisfied by the introduced complex coordinate transformation . Finally, on the PML external boundary a homogeneous Dirichlet condition is enforced,

$$\varphi = 0 \text{ on } \Gamma_E \ . \tag{18}$$

As the present work focuses on problems that are governed by the Helmholtz equation with spatially varying coefficients, the analytic continuation of the solution on the interface boundary between the computational region and the PML must be ensured in order for the latter to maintain its reflectionless properties. Hence, arbitrary variation of the effective

wavenumber is not technically allowed within the layer region. However, the PML is shown to be reflectionless for inhomogeneous media as long as they remain range independent within the layer along the direction perpendicular to the interface boundary (Oskooi et al., 2008). In the present contribution the above restrictions are easily met without any loss of generality, as it will be shown in Section 5 of the present work considering problems of water wave and hydroacoustic propagation.

3.2 Weak formulation

We consider the weight function $v\left(x_1, x_2\right)$ defined in the complex valued Sobolev space $v \in H_0^1\left(\tilde{\Omega};\mathbb{C}\right)$. Multiplying the field equation, Eq. (14) by the weight function v and integrating over the domain $\tilde{\Omega}$ results in,

$$\int_{\tilde{\Omega}}\left(\boldsymbol{\gamma}\bar{v}\nabla^2\varphi + k^2\gamma_1^{\lambda}\gamma_2^{\mu}\bar{v}\varphi\right)dx_1dx_2 = 0. \tag{19}$$

The overbar is used here to denote complex conjugation. Next, Eq. (19) is expanded and integration by parts is performed,

$$\begin{aligned}&-\int_{\Omega_*}\left(\nabla\bar{v}\cdot\nabla\varphi - k^2\bar{v}\varphi\right)dx_1dx_2 + \int_{\Gamma_S}\bar{v}\mathbf{n}\nabla\varphi\, ds + \int_{\Gamma_I}\bar{v}\mathbf{v}\nabla\varphi\, ds\\ &-\int_{\Omega_{\text{pml}}}\left(\nabla\left(\boldsymbol{\gamma}\bar{v}\right)\cdot\nabla\varphi - k^2\gamma_1^{\lambda}\gamma_2^{\mu}\bar{v}\varphi\right)dx_1dx_2 \; - \int_{\Gamma_I}\boldsymbol{\gamma}\bar{v}\mathbf{v}\nabla\varphi\, ds + \int_{\Gamma_E}\boldsymbol{\gamma}\bar{v}\mathbf{v}\nabla\varphi\, ds = 0\end{aligned}\quad . \tag{20}$$

At the PML interface Γ_I, the boundary terms cancel out due to the matching condition (17b). The external boundary term on Γ_E in Eq. (20) will vanish completely due to the imposed homogeneous Dirichlet condition on the external fictitious boundary. The boundary integral on the scatterer is computed using the corresponding incident wavefield data, and hence the weak formulation of the considered problems is obtained in the following form

$$\int_{\tilde{\Omega}}\left(\nabla\bar{v}\cdot\left(\boldsymbol{\gamma}\nabla\varphi\right) - k^2\gamma_1^{\lambda}\gamma_2^{\mu}\bar{v}\varphi\right)dx_1dx_2 = G\left(x_1, x_2\right) \equiv \int_{\Gamma_S}\bar{v}\mathbf{n}\nabla\varphi\, ds\ . \tag{21}$$

3.3 PML models

The classical choices for the functional form of the non-negative functions σ_i are polynomials of a varying degree with respect to a normalized coordinate within the layer,

$$\sigma_i\left(x_i\right) = \sigma\left[\frac{\left|X_i - x_i\right|}{\theta}\right]^n, \quad i = 1,2 \tag{22}$$

with coefficient $\sigma > 0$ and $n \geq 0$.

Increasing the value of σ and/or the degree n in Eq. (22) ensures a faster absorption within a given layer thickness θ . The above is merely translated to a larger imaginary part in the absorbing function (12) and larger but bounded integral in the transformation (11). However, increasing σ and/or n excessively results in an abrupt solution decay rate increasing artificial numerical reflections in the discretised form of the PML medium.

Moreover, enhancing the layer thickness is a means to achieve attenuation while keeping a slower decay rate, but would also result in an excessively enlarged computational domain and therefore enhanced computational cost. Collino and Monk (1998a) note the dependency of the optimal absorbing parameters on the employed mesh and the problem data. Hence, the application of effective PML-based techniques for truncating the computational domain, requires *a priori* tuning of those parameters. The criteria for establishing optimal PML parameters are not trivial and even then, the optimisation problem needs to be solved again after re-meshing (Bermudez et al., 2007).
In the present work, the optimal PML model for the scalar, reduced wave equation proposed by Bermudez et al. (2007) is adopted. The given model employs non-integrable profile functions of the form,

$$\sigma_i\left(x_i\right)=\left(\frac{1}{\left|X_i+\theta-x_i\right|}\right) \quad \text{for } x_i\in\Omega_{\text{pml}} \text{ and } i=1,2. \tag{23}$$

Instead of a bounded imaginary part, the absorbing function employing the profile of Eq. (23) results to an infinite integral in the complex coordinate stretching as seen in the comparative sketch of Fig.4

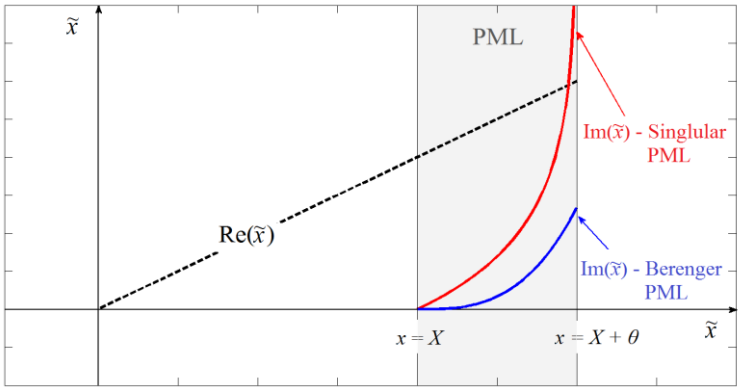

Figure 4. Sketch of the complex coordinate transformation Eq. (11).

The above has been proved to be optimal for the attenuation of plane wave solutions for the Helmholtz equation in infinite resolution (Bermudez et al., 2007), and also compares favorably against widely used polynomial forms; see Bermudez et al. (2007). Naturally, the absence of tunable parameters in Eq. (23) overcomes a major drawback of other PML methods. Cimpeanu et al. (2015) in their thorough investigation of the above singular PML model studied the effect of layer thickness, as the only remaining parameter controlling the performance of the layer. A rather interesting finding of their work is the existence of an optimal range of layer thickness values, within which the solution error becomes independent of the chosen thickness, thus rendering the singular PML model parameter-free for the scalar Helmholtz equation. In the present work the parameter-free, unbounded PML model will be implemented in a FEM strategy for the solution of the two linear elliptic problems with variable coefficients, rising in the fields of water-wave propagation and hydroacoustics, as presented above.

Published in Ocean Engineering - Volume 179, 1 May 2019, Pages 307-324

4 Numerical method

4.1 PML-FEM implementation

In this section we investigate the performance of the singular PML-FEM for the Helmholtz equation governing the problems under consideration. A series of numerical tests are conducted to determine the effectiveness of the method in simple configurations where analytical solutions are available. The analysis aims at establishing the robustness and limitations of the given methodology before its employment in the following applications of coastal engineering interest, (a) linear water wave refraction over mildly sloping bathymetries and in the presence of cylindrical bodies extending over the water column, and (b) acoustic wave propagation in the inhomogeneous ocean waveguide.

Standard conforming linear triangular elements $\left(p=1\right)$ are used in all examined cases. The method is clearly not restrictive of *p*-refinement, however the latter is outside the scope of the present study. We define the family of triangular partitions $\left\{T^h\right\}$ in domain $\tilde{\Omega}$ and φ^h denotes the finite element solution in $V^h \subset H_0^1\left(\tilde{\Omega};\mathbb{C}\right)$.

The approximate solution, restricted in the 3-node triangular element K, is

$$\varphi^h\Big|_{\mathrm{K}} = \mathbf{N}\boldsymbol{\varphi}_K^j, \tag{24}$$

where φ_K^j denotes the nodal unknowns and $\mathbf{N}=\begin{bmatrix}N_1 & N_2 & N_3\end{bmatrix}$ is a vector containing the linear Lagrange shape functions for the K element. The discretised weak formulation of problem (21) is thus written in matrix form as,

$$\int_{\mathrm{K}}\left(\left(\nabla\mathbf{N}\right)^T\boldsymbol{\gamma}\nabla\mathbf{N}-k^2\mathbf{N}^{\mathrm{T}}\gamma_1^{\lambda}\gamma_2^{\mu}\mathbf{N}\right)\boldsymbol{\varphi}_K^j\,dx_1dx_2=\mathbf{G}_K^h \tag{25}$$

where $\mathbf{G}_K^h$ assumes non-zero values, as defined in Eq. 16, when a K element edge lays on the scatterer boundary.

A Delaunay mesh is used for the discretisation of the computational region while a regular triangular grid is employed within the layer. The discretisation of the computational region is assessed by the number of employed elements per wavelength, in order to associate maximum element size with examined frequency. For the regular triangular mesh, the number of discrete segments employed along the transverse direction of the layer boundary, is used to denote the refinement inside the PML. A single segment, as seen in Fig. 5, results in two triangle faces with a common edge, corresponding to a diagonally divided quadrilateral element. The element matrices, in both the PML and the computational region, are computed numerically. The former in the PML region, contain the absorbing functions σ_i that become unbounded at the outer boundary, and the corresponding integrals involving the elements with an edge or a vertex at the outer boundary become singular. However, as shown by Bermudez et al. (2007) these integrals are either rendered finite due to the qualities of the Langragian shape functions which diminish at the outer boundary or become zero due to the imposed homogeneous Dirichlet condition at the external boundary Γ_{E}, which is proven necessary for the well-posedness of the discrete problem. Since the singularity is reached at the outer PML boundary the

Gauss-Legendre quadrature rule within the edge elements is applicable. A minimum of three integration points per element is employed to ensure that the presented analysis will not be polluted by numerical integration error.

In order to assess the performance of the FEM/optimal PML, the relative L_2 error norm of the approximation with respect to an available analytic solution, is defined as

$$\text{Error}=\frac{\left\|\varphi^h-\varphi\right\|}{\left\|\varphi\right\|},\quad \text{where}\quad \left\|\varphi\right\|=\left(\int_{\Omega_*}\bar{\varphi}\varphi\, dx_1dx_2\right)^{1/2}. \tag{26}$$

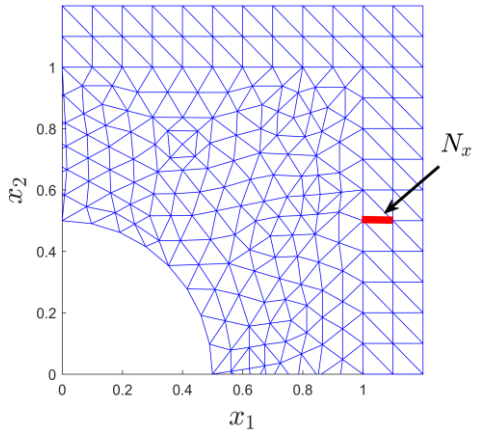

Figure 5. Mesh configuration with the PML regions $(x_1, x_2 > 1)$ discretized by two line segments along the transverse direction of the interface. A single line segment resulting in two triangles with a common edge is shown.

4.2 Numerical performance of the parameter-free PML-FEM

In order to establish the robustness of the presented method, a series of numerical experiments is carried out. First, the exterior scalar Helmholtz problem in $\mathbb{R}^2$, featuring a circular inclusion is considered. The investigation is carried out in the truncated domain $\Omega_r=(-5,5)\times(-5,5)$, featuring a unit circular scatterer centered at the axes origin. Two cases of incident wavefields on the circular scatterer with radius *a* are considered.

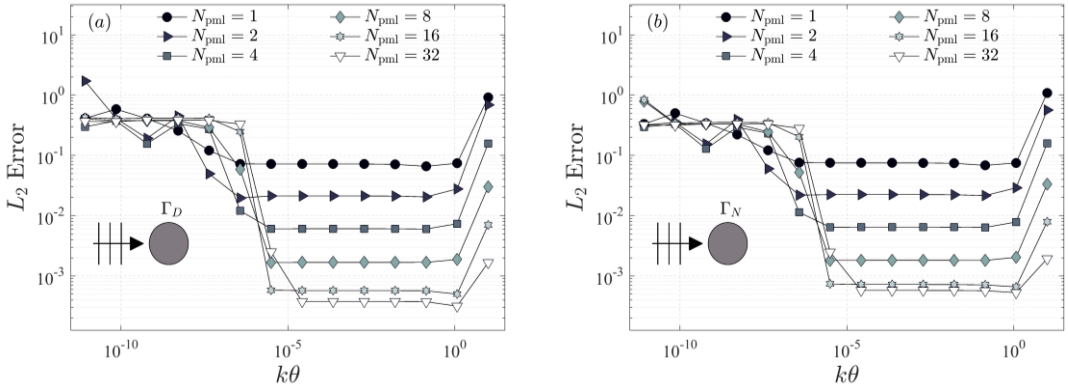

Figure 6. Calculated error of the scattered field by a circular body, $ka=1$, in the case of incident plane waves. Results for various normalised PML thickness values and increasing PML discretisation: (a) soft scatterer, (b) hard scatterer. A total number of elements $N/\lambda=88$ is employed for the discretization of the computational region.

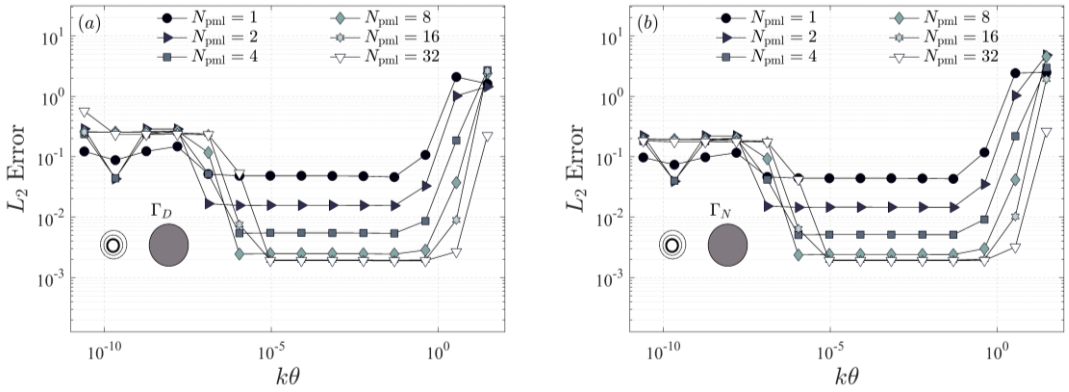

Figure 7. Calculated error of the scattered field by a circular body, $ka = 3$, in the case of waves emitted from point source. Results for various normalised PML thickness values and increasing PML discretisation: (a) soft scatterer, (b) hard scatterer. A total number of elements $N/\lambda = 53$ is employed for the discretization of the computational region.

The first is the case of parallel plane wave incidence, i.e. $\Phi_i = \exp(ik\mathbf{x})$, for which the singular PML is shown to be optimal, and the second is the incidence of a wavefield generated by a monopole, i.e. $\Phi_I = H_0^{(1)}\left(k\left|\mathbf{x}-\mathbf{x}_s\right|\right)$ positioned at $\mathbf{x}_s / a = (-3,0)$. Assuming a uniformmedium, i.e. $k = const$, the solutions for the two incident wave cases are calculated analytically and used for validation of the employed PML-FEM. Analytical solutions are documented in the Appendix; see Figs A.1 and A.2.
The effect of normalized absorbing layer thickness is initially considered. The relative errors for solutions with a fixed discretization in the computational region are plotted against a range of layer thickness values, $10^{-12} \le k\theta \le 10^{1}$ in Figs. 6 and 7.
Different curves correspond to an increasing number of triangular elements in the PML region. Two different wave numbers are examined for $ka = 1$ and 3. In both cases the discretization of the computational region is kept constant. It is observed that for all examined cases and a given discretization in the computational region and in the PML, there exists an optimal range of thickness values for which the error is independent of further increase of layer thickness.

The above result, which is in agreement with similar findings by Cimpeanu et al. (2015), suggests that the singular PML is highly effective for rather small thicknesses that are orders of magnitude smaller than the excited wavelength in this monochromatic case. The significance of the above result lays in its immediate translation in reduced degrees of freedom for a given level of accuracy. The presented results in Figs 6 and 7 show optimal thickness values within the range $10^{-4} < k\theta < 10^{-1}$, depending on the discretization employed in the layer, i.e. N_{pml} . The error increases dramatically as $k\theta$ becomes large (becomes of order 1 or higher) in the given examples. This is attributed to the crude discretization in the layer, indicating that the restriction on the upper boundary of accepted PML thickness values for a given k is posed by the number of employed elements in the layer. In fact, increasing the number of elements in the layer resulted in enhanced optimal value ranges as seen in Figs. 6 and 7. Additionally, the rapidly increasing error after the

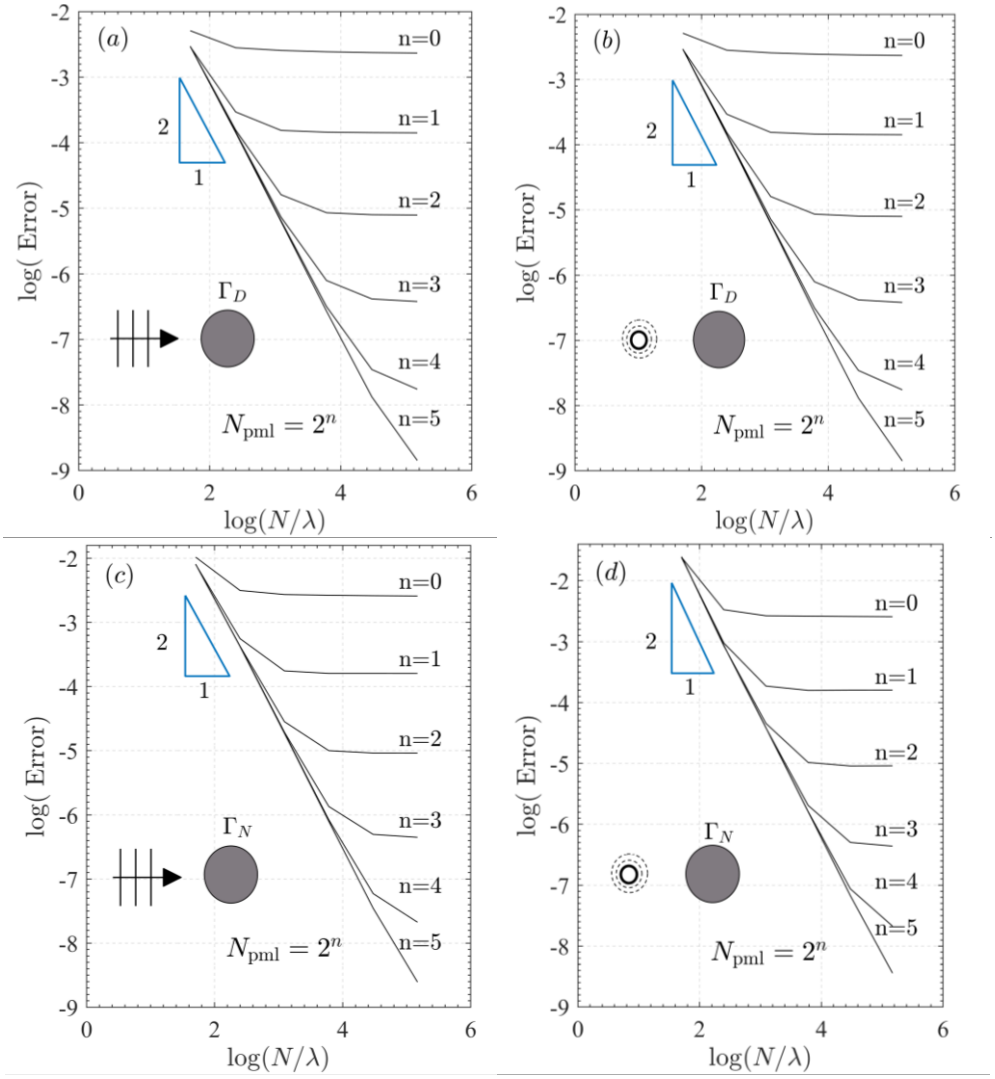

Figure 8. Calculated error of the scattered field by circular body, $ka = 1$, against the number of elements per wavelength for increasing number of elements employed in the PML subregion. Soft scatterer boundary for (a) incident plane and (b) a source generated wavefield. (c) and (d) Similar as before for hard scatterer.

lower limit of the optimal value range of $k\theta$ is attributed to the error associated with numerical integration. Furthermore, increasing the discretization within the layer appears to improve the calculated error plateau as clearly shown in both Figs. 6 and 7. However, in finer meshes within the layer, employing $N_{\text{pml}} = 16$ and $N_{\text{pml}} = 32$, the consistent reduction in the calculated error plateau reaches to a halt, suggesting that the error introduced by the discretization in the computational region becomes increasingly dominant. The above observation is verified by the convergence of the method. For the previous cases, log-log plots of the relative error L_2 norm, against an increasing number of elements per wavelength are shown in Figs. 8 and 9 for $ka = 1$ and $ka = 3$, respectively, for PML thickness $k\theta = 10^{-4}$ within the established optimal range. Notably, the chosen value of normalised thickness corresponds to an extremely thin layer compared to wavelength as it holds $\theta \simeq \lambda/62800$. It is seen that, by refining the mesh in the computational region, the error introduced by the PML discretisation becomes dominant. However, increasing the number of elements within the layer further reduces the error and

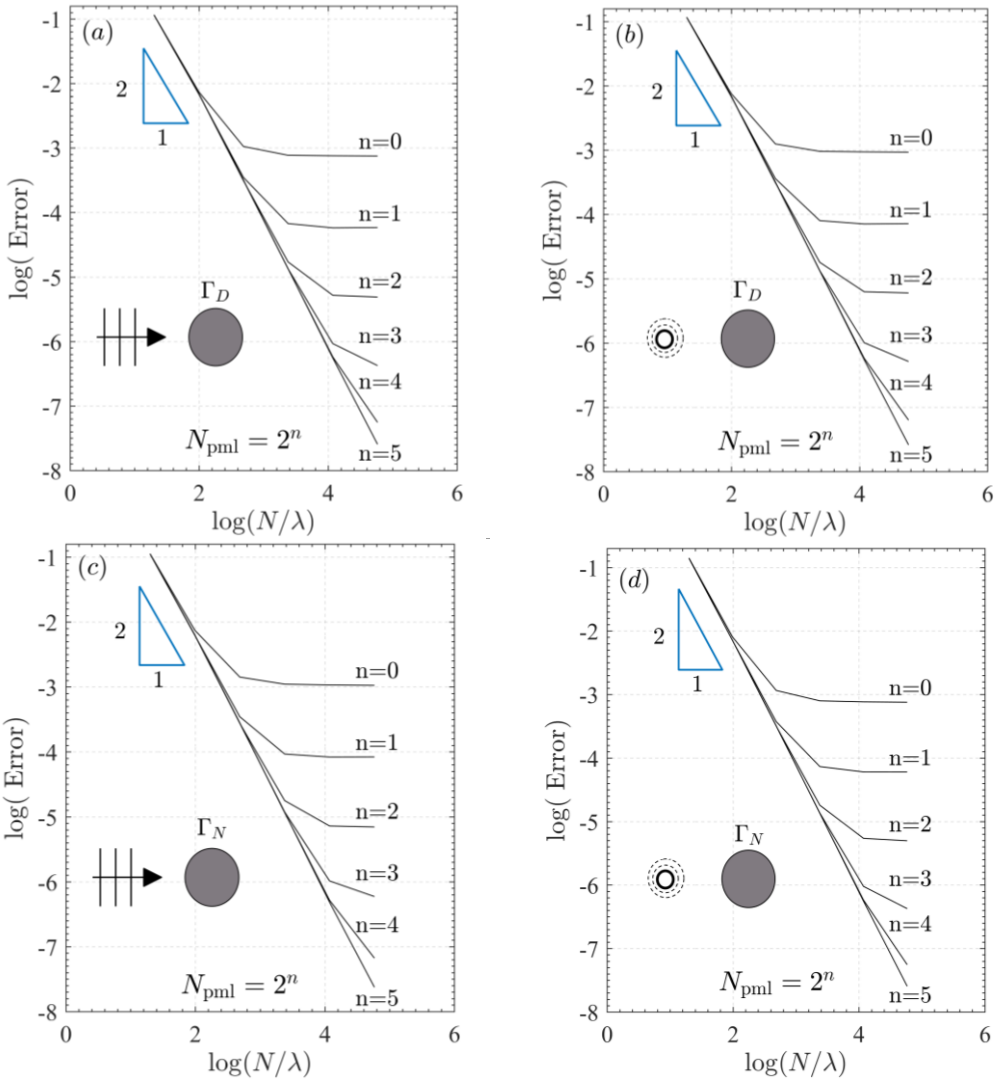

Figure 9. Calculated error of the scattered field by a circular body, $ka = 3$, against the number of elements per wavelength for increasing number of elements employed in the PML subregion. Soft scatterer boundary for (a) incident plane and (b) a source generated wavefield. (c) and (d) Similar as before for hard scatterer.

recovers the theoretically expected convergence rate, which for linear elements is $\left\|\varphi^h - \varphi\right\| < C\left(N/\lambda\right)^{-2}$. The theoretical convergence slope 2:1 is shown the Figs. 8 and 9 for comparison.

The convergence rate depends on both the computational region discretisation and the refinement within the layer. The fact that the effectiveness of the singular PML is independent of the employed mesh structure and requires no *a priori* tuning, as opposed to polynomial choices for the absorbing function, in conjunction with the above results, suggests that a required level of accuracy can be achieved with little effort. Additionally, the calculated optimal range allows for a layer thickness value that is orders of magnitude smaller than the examined wavelength, and thus, the present method does not result in an excessive augmentation of global FEM matrices.

4.3 Numerical performance for scattering problems in a waveguide

Next, the radiating field from a point source in a waveguide is considered. In absence of analytical solutions for the scattering problem in simple waveguides featuring an inclusion, we employ a radiating solution produced by a line source to compute the Dirichlet data on the boundary of a fictitious scatterer enclosing the source. We consider the unbounded homogeneous waveguide in $\Omega_S = (-\infty,\infty)\times[-h/2,h/2]$ with imposed Neumann conditions on the top and bottom planar boundaries Γ_B:

$$\frac{\partial\varphi(x_1,-h/2)}{\partial x_2} = \frac{\partial\varphi(x_1,h/2)}{\partial x_2} = 0. \tag{27}$$

The analytical solution of the incident wavefield is expressed by normal mode series, and the vertical structure of the modes corresponding to the eigenvalues $k_{x_2 n}$ is chosen as $Z_n(x_2) = \cos\left(k_{x_2 n}(x_2 + h/2)\right)$ in order to satisfy the Neumann conditions (27) on the planar boundaries. Details are provided in the Appendix; see Eq.(A.10) and Figs.A3 and A.4. The series (A.10) can be truncated, keeping the propagating and a number of evanescent modes sufficient for rapid convergence in the whole region outside a small ball in the vicinity of the line source, i.e. $kr = \sqrt{(x-x_0)^2+(y-y_0)^2} > \varepsilon$. Assuming the presence of a circular scatterer with center (x_0, y_0) enclosing the line source, boundary data are calculated at $r = a$, where a is the radius of the scatterer. The PML-FEM radiating field in the waveguide generated by the imposed Dirichlet condition is compared to the analytical solution (A.10) outside the circular scatterer. Results are obtained in the domain $\Omega_s : [-16\alpha, 16\alpha]\times[-5\alpha, 5\alpha]$ for $k\alpha = 1$, and the effect of normalized PML thickness is initially examined in Fig. 10.

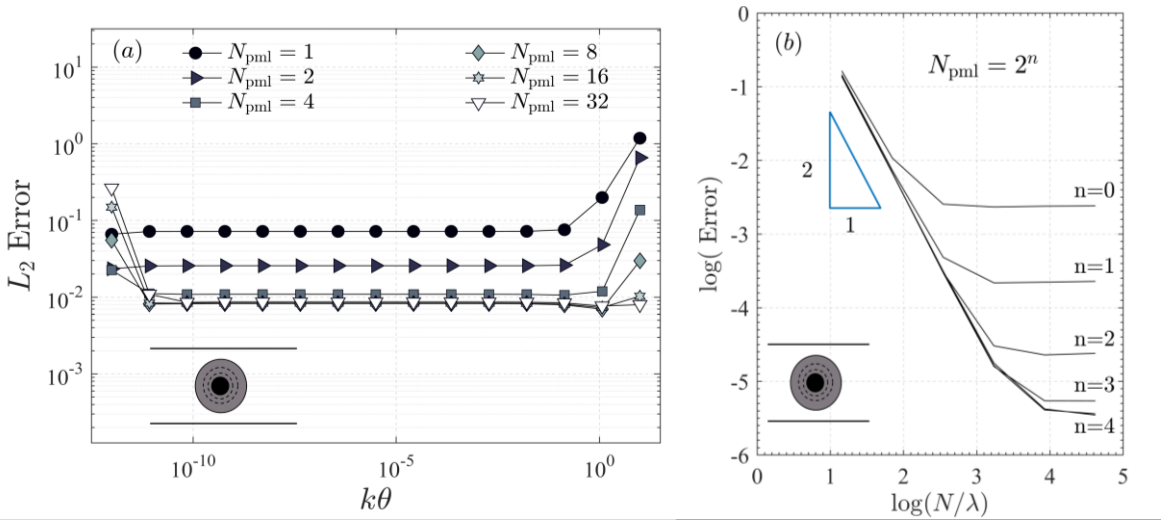

Figure 10. Radiating field outside a circular scatterer in a planar waveguide, for *ka*=1. (a) Parametric study of the calculated error for a range of normalised PML thickness values and increasing PML discretisation in the waveguide environment. (b) Calculated error of the scattered field by circular body, against the number of elements per wavelength, and for increasing number of elements employed in the PML.

Again, a range of optimal layer thickness values is observed, which is now $10^{-10} < k\theta < 10^{-1}$. Similar to the previous example, the theoretical rate of convergence is revealed by increasing the number of elements in the PML region.

5 Water-wave diffraction and acoustic scattering applications

5.1 Water-wave propagation over sloping seabed with an elliptic shoal

The presented PML-FEM strategy will be initially implemented in the study of linear water wave propagation phenomena in a mildly sloping ocean environment. The MMS equation, as presented in Section 2, will be employed for the formulation of the combined refraction-diffraction problem. The numerical solution will be compared against a test case of diffraction by an elliptic shoal superimposed over a sloping bottom bathymetry. Next, the capabilities of the computational tool will be demonstrated for the case of a single and multiple bottom founded cylinders. Subsequently, the numerical solution of the acoustic scattering problem by an elliptic obstacle in the complex ocean waveguide will be considered.

The MMS model featuring the unbounded PML will be tested against the laboratory data concerning monochromatic wave propagation over a submerged elliptic shoal superimposed over a sloping seabed, presented in Berkhoff et al. (1982); see also Dingemans (1997). The elliptic shoal presents a standard benchmark problem for the validation of numerical schemes aiming at the accurate prediction of combined refraction-diffraction phenomena. The analysis presented in Section 2.1 for the case of a mildly sloping bathymetry supporting a localised, submerged scatterer is followed. A monochromatic wave with period $T = 1\,s$ and initial wave amplitude $A_0 = 2.32$ cm is allowed to propagate parallel to the x-axis in angle $\theta_I = 20^\circ$ with respect to the minor axis of the elliptic shoal. It is stressed here that, results obtained by the present linear model are not dependent on the wave amplitude. However, as a next step in our analysis, a nonlinear correction in the dispersion relation will be applied accounting for amplitude effects. The underlying plane slope is given by,

$$h_i(x) = \begin{cases} 0.45m, & x < -5.85m \\ 0.45 - 0.02(5.85 + x)\,m, & -5.85m \le x \le 14.15m \\ 0.05m, & x > 14.15m \end{cases} \tag{28}$$

The localised elliptic shoal, seen as a disturbance on the background bathymetry h_i is described as,

$$h_d(x,y) = \begin{cases} 0, & (x/3)^2 + (y/4)^2 > 1 \\ 0.3 - 0.5\sqrt{1 - (x/3.75)^2 - (y/5)^2}, & (x/3)^2 + (y/4)^2 \le 1 \end{cases} \tag{29}$$

The diffracted potential Φ_d is obtained by the numerical solution of the reduced MMS Eq.(3) over the superimposed bathymetric profiles (28) and (29). Finally, a PML enclosing

the region of computational interest, defined in Eqs. (14) and (15), will model the absorption of wave energy reaching the exterior termination boundary.

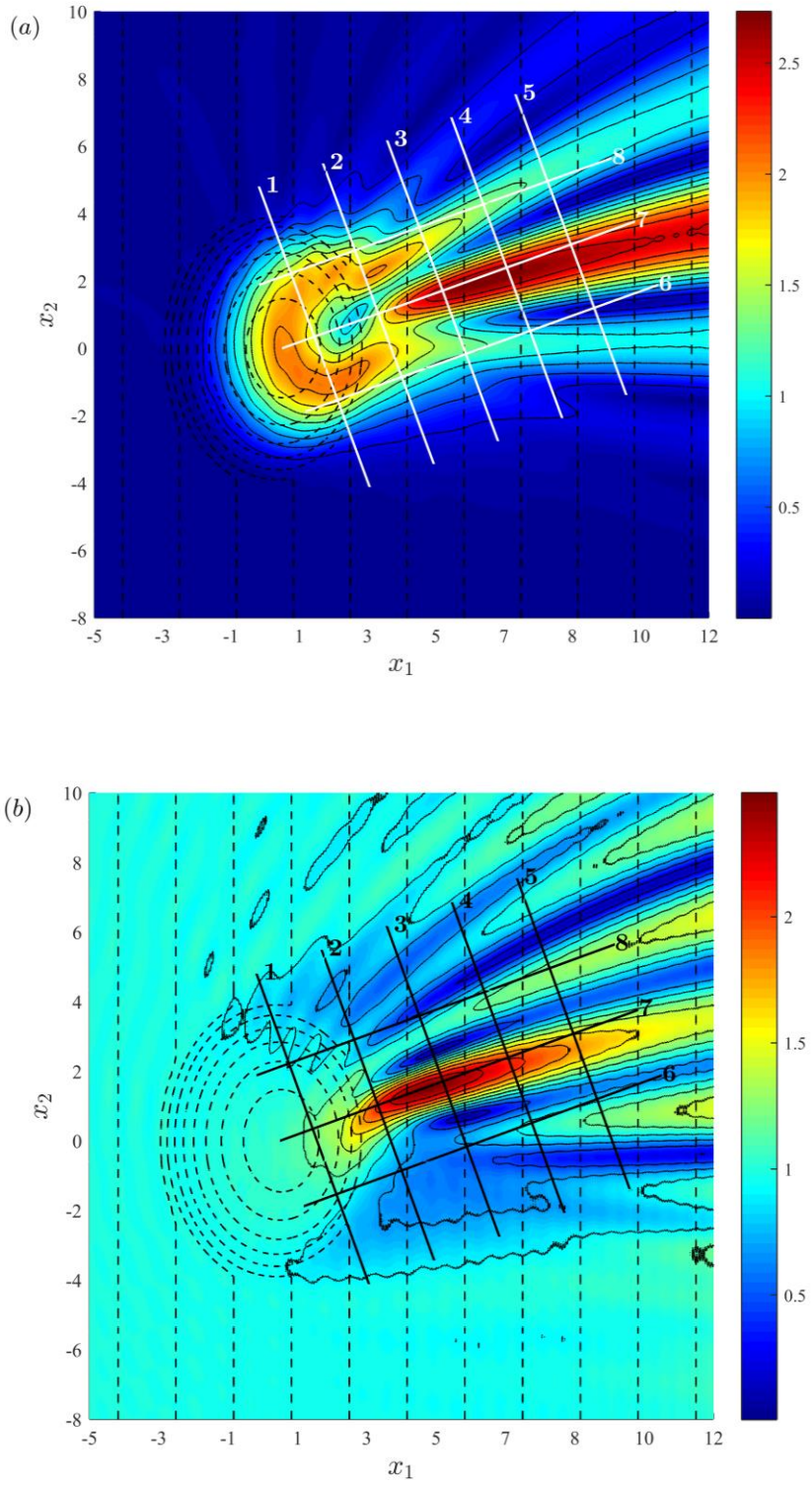

Figure 11 (a) Modulus of the diffracted wavefield, calculated by the present PML-FEM method. (b) Modulus of total wavefield. The sections corresponding to the experimental setup in Berkhoff et al. (1982) are indicated by solid lines.

It is reminded that Eq.(3) is a quasi linear elliptic equation with the effective wavenumber dependent on the depth function through the dispersion relation $\omega^2 = k(x,y)\, g \tanh\left[k(x,y)h(x,y)\right]$. The bathymetric profile, defined as the superposition of Eqs. (28) and (29), satisfies the restrictions imposed on the coefficients of the MMS in order to preserve the PML analytic continuation (Sec. 3.1). The layer is used to truncate the computational region at $x_1 = -6m$ and $x_1 = -16m$ hence the depth function is kept constant in the vertical PML regions. In the horizontal PML regions the depth function exhibits variation only along the x coordinate, thus remaining constant in the direction perpendicular to the horizontal boundaries, as imposed by Eq (28). The latter ensures the reflectionless characteristic of the PML (Oskooi et al., 2008).
The use of the MMS equation for modelling combined refraction-diffraction phenomena subscribes to the limitations of small amplitude water wave theory, which fails to capture the complex diffraction pattern behind the elliptic shoal. For the numerical experiment a PML thickness $k\theta = 4.2\ 10^{-4}$, corresponding to the established optimal range is used. A quasi-uniform Delaunay mesh is employed in the region of computational interest while a uniform triangular mesh is used for the PML (see Fig. 5). A total of 16 line segments were employed for the discretisation of the absorbing layer and a total of $1.2\ 10^6$ nodes (discrete unknowns) were used to ensure the convergence of the numerical solution in the present example. The diffracted and total wave potential moduli, calculated using the linear dispersion relation, are plotted in Fig 11. In particular, in Fig. 10(a), the diffracted wavefield solution is illustrated which compares well with similar solutions from the literature (e.g., Panchang et al., 1991; Belibassakis et al., 2001), exhibiting smooth equal amplitude lines for the modulus, suggesting that outgoing solutions are properly attenuated by the present PML model. As expected, due to its inability to account for nonlinear processes, such as energy dissipative mechanisms, the MMS model overestimates the wave amplitude behind the shoal (sections 2, 3 and 4) while it attenuates the solution faster moving away from the shoal.
Next, the computed wave amplitude for various sections is compared against the experimental data in Fig. 12, for sections 2-4 and 6. Although present results corresponding to the linear solution shown by dashed lines reproduce fairly well the experimental measurements, an updated prediction is also shown in Fig.12 based on the work by Kirby and Darlymple (1986).

The latter proposed a correction of the wavenumber-parameter of the mild-slope equation in order to take into account amplitude effects at first-order, as follows

$$\omega^2 = gk\left[1+(kA)^2\ f_1 \tanh^5(kh)\right]\tanh\left[kh+(kA)\ f_2\right] \tag{30}$$

where $f_1 = \dfrac{\cosh(4kh)+8-2\tanh^2(kh)}{8\sinh^4(kh)}$ and $f_2 = \left(\dfrac{kh}{\sinh(kh)}\right)^4$. (31)

The above amplitude-dependent dispersion relation generates results that compare more favourably with measured data as shown in Fig.12 by the use of solid lines.

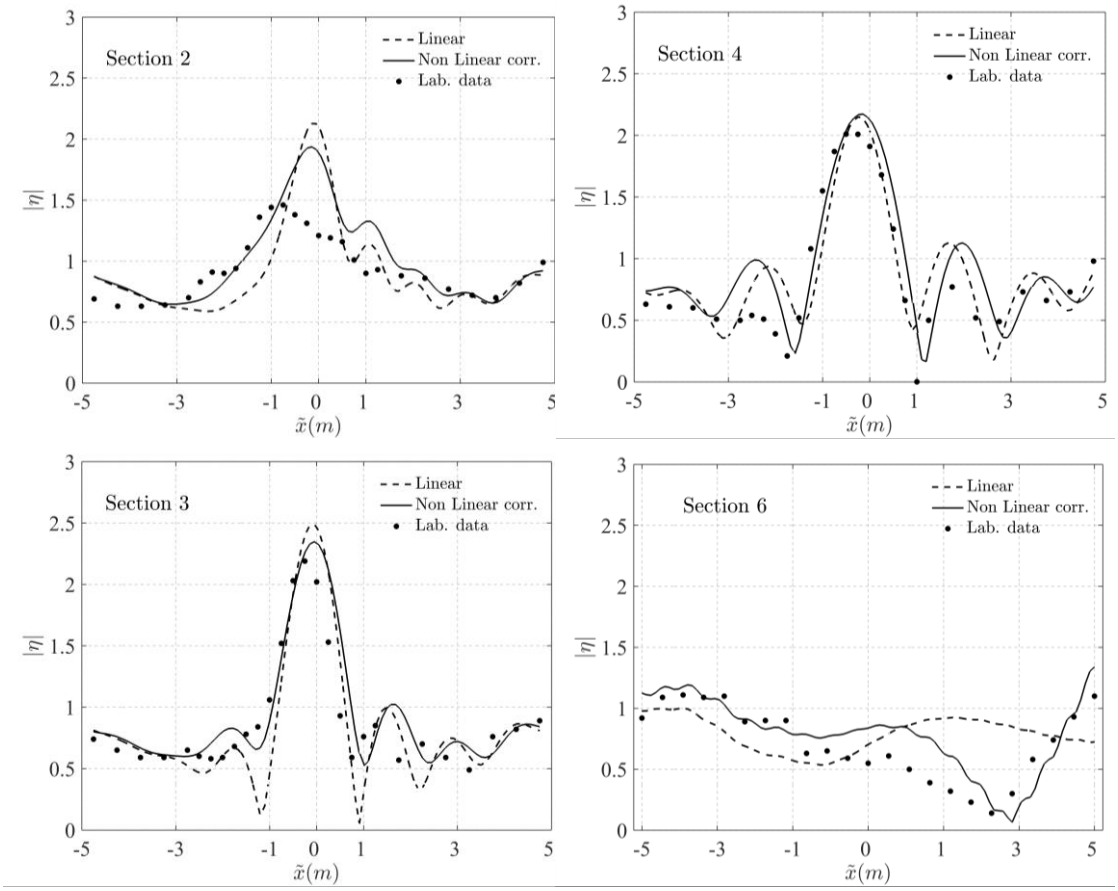

Figure 12. Normalised amplitude on selected sections over the elliptic shoal. Comparison of the present PML-FEM solution, shown by dashed line, against the experimental data of Berkhoff et al.(1982) denoted by dots. In the same plots the solution featuring the amplitude corrected dispersion relation are shown by using a solid line

In particular, a number of 5 consecutive iterations were performed updating the predicted wave amplitude and the wavenumber parameter; see also Panchang et al., 1991). The nonlinear correction provides better matching of numerical results with the experimental data, particularly concerning the peak amplitude values for sections 2, 3 and 4 and a marked improvement on the solution at section 6.

5.2 Diffraction by vertical cylinders in variable bathymetry region

The accurate prediction of wave transformations and induced loads in the presence of manmade structures or physical formations finds several engineering applications. In this subsection the multiple scattering of an array of bottom-founded cylinders over a mildly sloping seabed is considered. The bodies extend along the water column. For the following analysis, the same bathymetric profile, defined by Eq. (28), i.e. a seabed with constant slope 2% is used. An oblique incident wavefield with nondimensional frequency $\omega^2 h g^{-1} = 1.8$, propagating from the deep water region is refracted over the sloping seabed topography and interacts with a single bottom founded cylinder with circular cross section. As in the previous subsection, the numerical solution for the diffracted wavefield Φ_d is derived by means of the reduced MMSE, defined in Eq.(4). Use is made of condition (5) on the scatterer surface boundary and the propagating wavefield

Φ_i over (28). Again, a PML enclosing the region of interest, defined in Eqs.(14) and (15), models the absorption of wave energy reaching the exterior termination boundary.

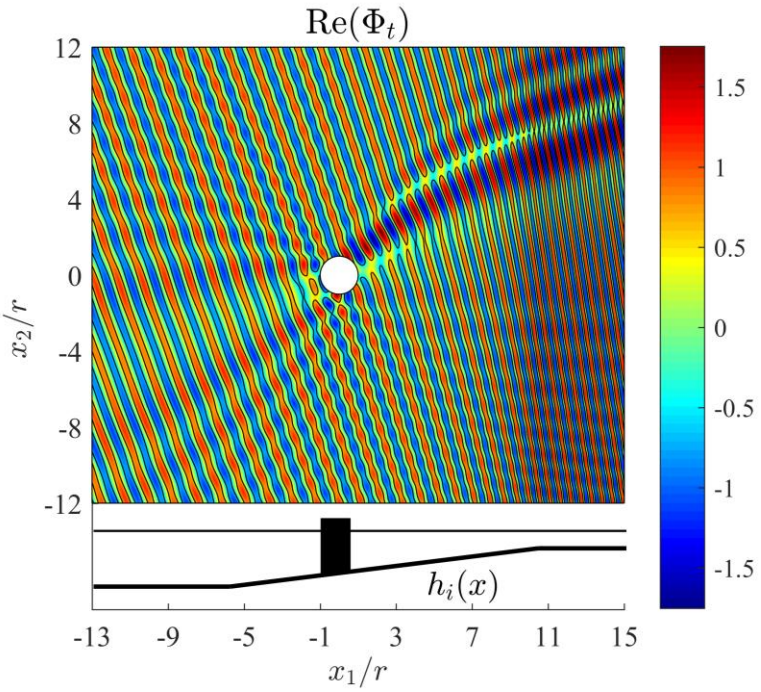

Figure 13. A single vertical cylinder with rigid walls (Neumann boundary condition) over a linear bottom slope for the case of an incoming, incident wave of nondimensional frequency $\omega^2 h g^{-1} = 1.81$ and angle of incidence $\theta = 20^{\circ}$.

Figure 13, depicts the real part of the total wave potential field for the cases of imposed (a) Dirichlet and (b) Neumann conditions on the scatterer boundary. Similar to the above case, a Delaunay-uniform triangular hybrid mesh is employed and as before, the thickness of the employed PML is set to $k\theta = 4.2\ 10^{-4}$, with 16 line segments in the direction normal to the layer boundary. In this case a total of 90163 nodes were employed for convergence. The drawn axes are normalized with respect to the cylindrical scatterer (pillar) radius. The plotted solutions show no contamination from spurious numerical reflections, suggesting once again the effectiveness of the employed singular PML. The total wavefield is refracted as it propagates towards shallower regions, with the wavelength decreasing up to the constant shallow depth limit. Next, the robustness of the present model in multiple scattering problems within variable bathymetry regions is demonstrated. Figure 14 depicts the complex total wavefield, resulting from the interaction of the same oblique, incident wave as in the previous example with the same sloping bathymetry and an array of nine bottom founded cylindrical scatterers with circular cross section. The layer thickness remains the same as in the previous example. The entire domain is shown in Fig. 14a, excluding the attenuating layer.

Figure 14b focuses on the complex, amplified wavefield patterns that appear close to the array, while Fig. 14c illustrates the satisfaction of the imposed zero Neumann conditions for the total wavefield at the boundary of the central scatterer.

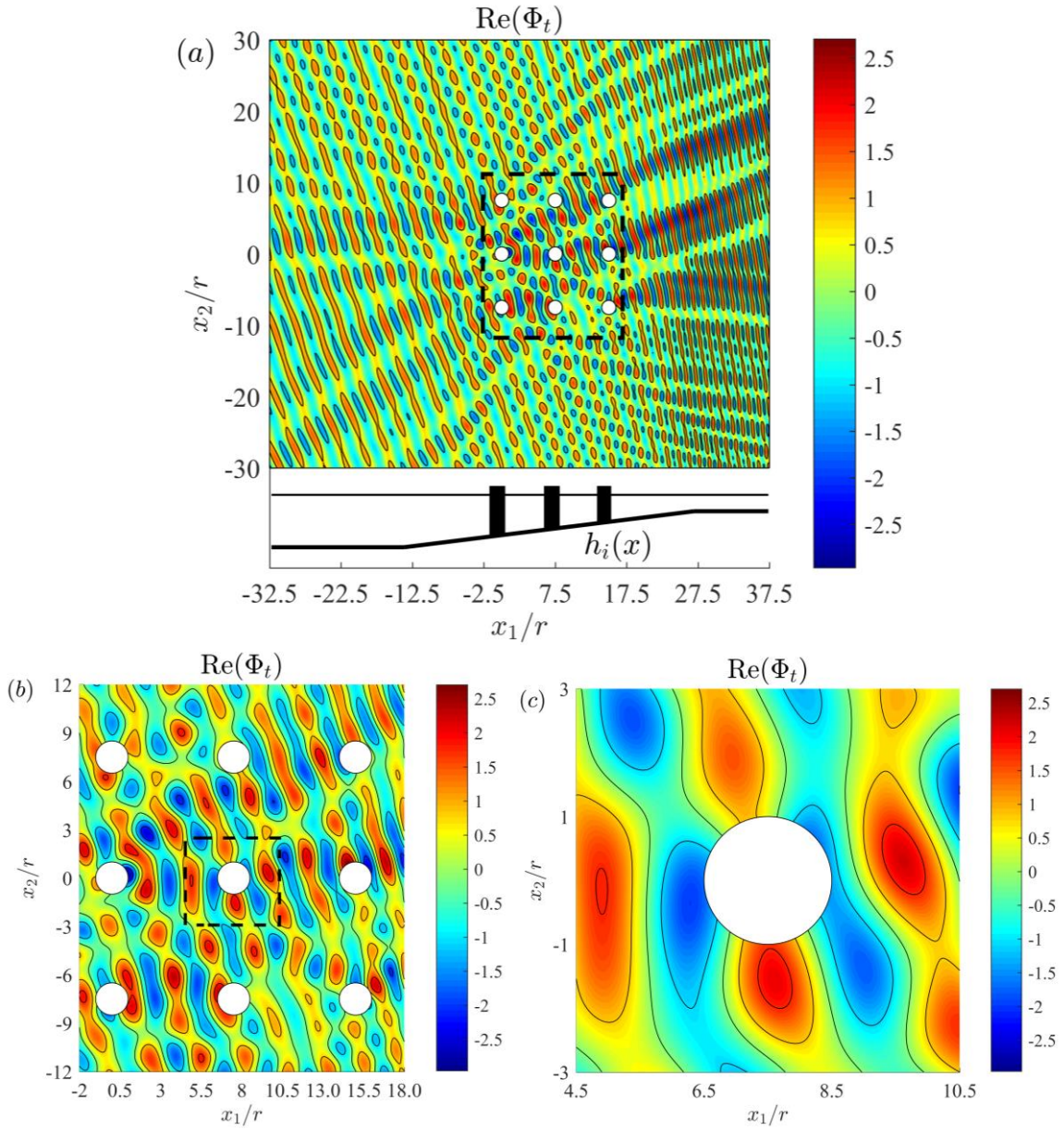

Figure 14. An array of nine vertical rigid cylinders over a linear slope for incident wave of non-dimensional frequency $\omega^2 hg^{-1} = 1.8$ and obliquely incident waves $\theta_I = 20^\circ$. (a) total domain, (b) focus on the array scale, (c) plot around a central cylinder.

5.3 Acoustic scattering by an elliptic body in a planar waveguide

Here, a homogeneous waveguide with planar boundaries $\Omega_s : [0, 400m] \times [-100m, 0]$ is considered excited by a line source located at $(0, -10m)$. The acoustic medium in this example is water and the phase speed is c =1500m/s. The scattering field from an elliptic body with major and minor axis $A = 16m$ and $B = 4m$, respectively, in the middle of waveguide is considered; see Figs.15,16. The elliptic geometry of the acoustic scatterer was chosen to both illustrate the capability of the finite element mesh to capture curved boundaries and to simulate common ocean underwater vehicle shapes.

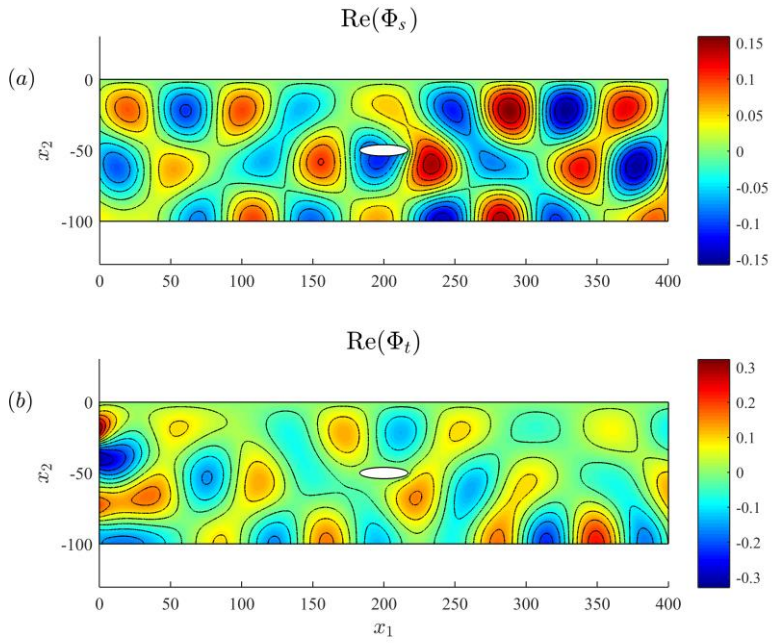

Figure 15. Real part of the scattered field and total wavefield solution in the case of an acoustically soft body (Dirichlet boundary condition) with elliptic boundary, for *kA* =1.7.

Solving the Helmholtz equation, Eq. (9), defined on the vertical plane, and forced by a monochromatic point source yields the scattered field solution Φ_s. Moreover, the free surface boundary condition Eq.(7a), the rigid bottom boundary condition Eq.(7b) and the PML Eq.(14) modelling absorption of wave energy reaching the termination boundaries at the lateral edges of the domain, *x*=0 and *x*=400m are employed. The boundary conditions, supplementing the hydroacoustic problem in the waveguide correspond to a free upper surface boundary and an acoustically hard, impermeable sea bottom. The real parts of the diffracted and total acoustic wavefields for the cases of an acoustically hard and soft scatterer boundary are shown in Figs. 15 and 16, for *kA* =1.7. PML regions with thickness $k\theta = 10^{-6}$ are positioned at the lateral domain boundaries, while 16 line segments along each region are employed. A total of 133856 nodes are employed for this example. It is clear that the present PML-FEM strategy is able to handle arbitrary scatterer shapes, with the tradeoff being the required *h*-refinement to handle complex geometries. Moreover, it is clearly observed with the aid of the contour plots of the diffracted wavefield in Figs. 15 and 16 that the boundary conditions on the surface of the body are very well satisfied, and although this test case is a rather simplified example, the present method is directly applicable to more realistic cases in general stratified environments and mixed –type boundary conditions on the surface of the scatterer(s).

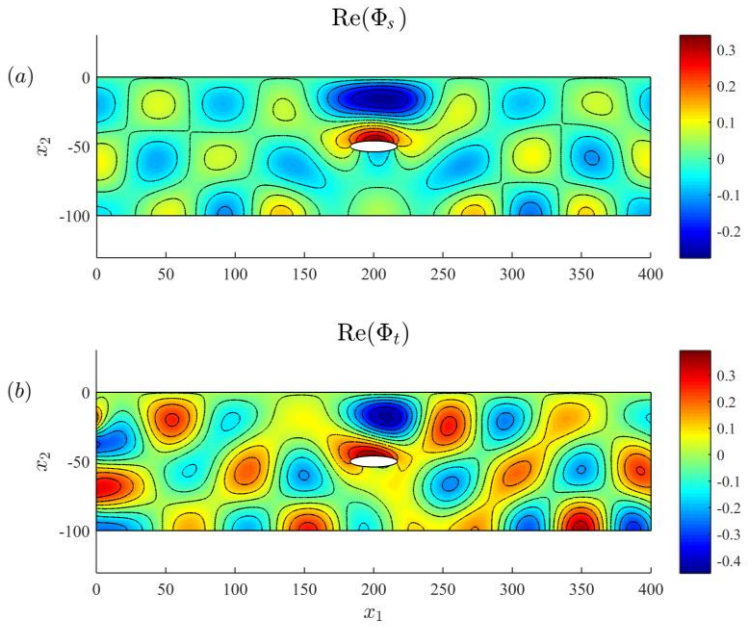

Figure 16. Scattered and total wavefield, as in Fig.15, for an acoustically hard scatterer (Neumann boundary condition).

6 Conclusions and future work

The scattering problem governed by the Helmholtz equation with spatially variable coefficients is studied in the context of refraction-diffraction and scattering phenomena in the ocean environment. After establishing the mathematical similarities between the problems of water wave propagation in mildly-sloped variable bathymetry regions and hydroacoustic propagation in the inhomogeneous infinite strip resembling the sea-coastal waveguide, a unified PML-FEM strategy is developed for numerical simulation. The effectiveness of the parameter-free PML model, featuring a singular absorbing function was examined against known analytical solutions. The singular PML for a hybrid regular-Delaunay triangular, finite element mesh was studied for a range of thickness values in both problem cases, with very good results, indicating the effectiveness of the present method for problems involving the Helmholtz equation with variable coefficients. The advantages of the employed absorbing function lay on the fact that it requires no *a priori* tuning, as is the case for classical, polynomial function forms. Additionally, a layer of thickness several orders of magnitude smaller than the characteristic wavelength, is highly effective, resulting in minimal computational cost compared to standard PML adaptations. Finally, the present results are compared against experimental data in the case of water-wave propagation over an uneven seabed with the presence of an elliptic shoal, and numerical examples are illustrated in applications involving diffraction by vertical cylinders in variable bathymetry regions and scattering by an elliptically shaped body in the sea-acoustic waveguide. Based on the preceded analysis and demonstrative examples, the presented singular PML is a very promising alternative due to its low computational cost, simplicity in FEM implementations and achieved efficiency.

Published in Ocean Engineering - Volume 179, 1 May 2019, Pages 307-324

Appendix. Benchmark solutions

First, specific analytical solutions of scattering problems by cylindrical bodies in $\mathbb{R}^2$ are reviewed, then simple outgoing solutions in the planar waveguide are presented, in order to be used for error calculation and the evaluation of the present PML-FEM. In particular the scattered wavefields on the circular inclusion surface are calculated for the case of an incident plane wave, as well as for an incident wavefield generated by a point source. For the scattering problem in the infinite strip, with homogeneous Neumann conditions on the planar boundaries, an analytical solution can be devised by means of a rapidly convergent normal mode expansion series.

(a) Scattering fields by a cylindrical obstacle

The scattered wavefield by a cylinder with surface Γ_S and radius a, is obtained as the solution to the exterior Helmholtz problem with constant parameter k in the open two-dimensional domain $\Omega = \left\{ x_i \in \mathbb{R} \ : r = \left(x_1^{\,2} + x_2^{\,2} \right)^{1/2} > a \right\}$.

$$\nabla^2 \varphi_s + k^2 \varphi_s = 0 \ , \ \text{in} \ \ \Omega \quad , \tag{A1}$$

$$\alpha \frac{\partial \varphi}{\partial n} + \beta \varphi = -\left(\alpha \frac{\partial \Phi_i}{\partial n} + \beta \Phi_i \right) \ \text{on} \ \Gamma_S \tag{A2}$$

$$\lim_{r \to \infty} \sqrt{r} \left(\frac{\partial \varphi}{\partial r} - ik\varphi \right) = 0 \, . \tag{A3}$$

which ensures that waves are outgoing at infinity (Sommerfeld condition for $r \to \infty$). The known data f on the scatterer surface are defined from the incident wavefield Φ_I. The representation of the solution is given by (see, e.g., Mei 1994)

$$\varphi(r,\theta) = \sum_{m=0}^{\infty} A_m \cos(m\theta) H_m^{(1)}(kr) \ , \tag{A4}$$

where $H_m^{(1)}$ are the Hankel functions of the first kind and m order. The coefficients A_m are dependent on the imposed boundary condition on the scatterer surface Γ_S and the incident wavefield. In the case of plane incident wave (see Fig.A1a) the analytical solution of the scattering field, for a acoustically soft and hard boundary, respectively, is given by

$$A_m = -e_m i^m \frac{J_m(ka)}{H_m^{(1)}(ka)} \quad \text{and} \quad A_m = -e_m i^m \frac{J'_m(ka)}{\Phi_m^{(1)}(ka)} . \tag{A5a}$$

where e_m denotes the Neumann symbol, $J'_m(\cdot) = dJ_m(\cdot)/d(\cdot)$ and $\Phi_m^{(1)}(\cdot) = d\mathrm{H}_m^{(1)} / d(\cdot)$.

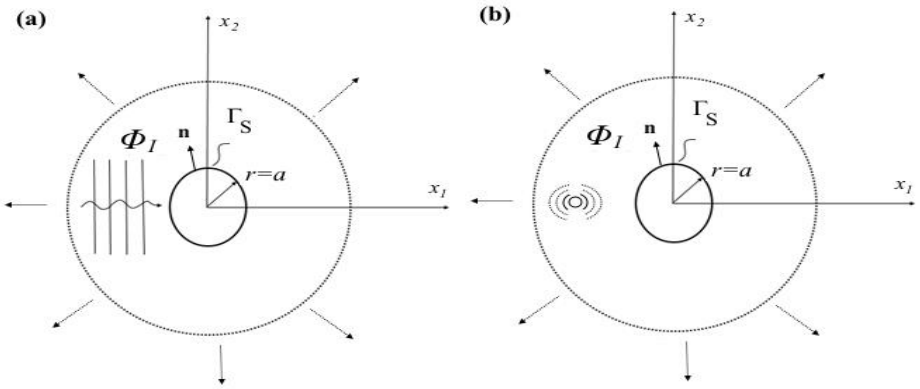

Figure A1. The exterior Helmholtz problem with a circular inclusion in $\mathbb{R}^2$. (a) Plane wave incidence, (b) Wavefield generated by a point source.

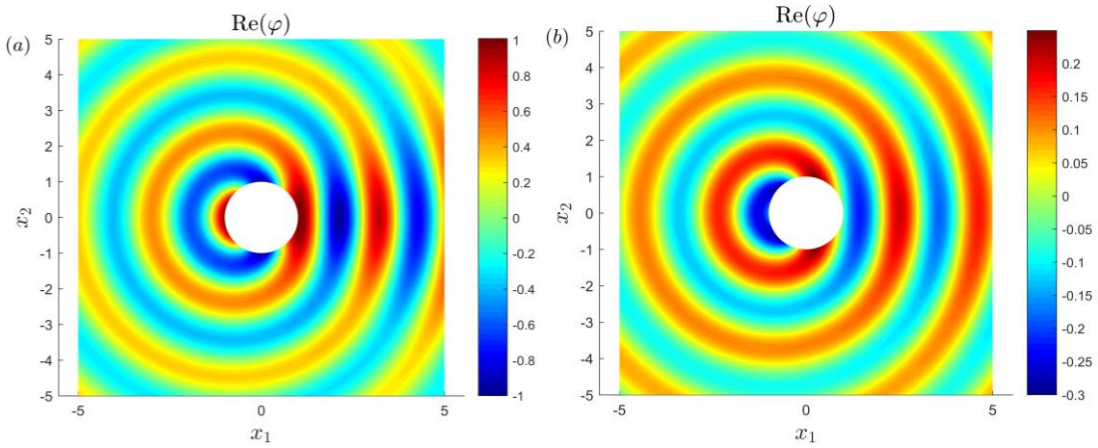

Figure A2 (a) Real part of the scattered velocity potential φ with $\Phi_I = \exp(ik\mathbf{x})$ and (b) $\Phi_I = H_0^{(1)}\left(k\left|\mathbf{x}-\mathbf{x}_s\right|\right)$, for ka=3 and Dirichlet conditions on the scatterer boundary.

In the case of an incident wavefield generated by an acoustic source located at a distance s from the center of the circular scatterer (see Fig.A.1b) the corresponding coefficients are,

$$A_m = -e_m(-1)^m \frac{H_m^{(1)}(ks)\,J_m(ka)}{H_m^{(1)}(ka)} \quad \text{and} \quad A_m = -e_m(-1)^m \frac{H_m^{(1)}(ks)\,J_m'(ka)}{\Phi_m^{(1)}(ka)} \quad . \tag{A5b}$$

See e.g., Martin (2005). Indicative solutions are shown in Fig. A2.

(b) Analytical solution in a planar waveguide

Next, a scattering field in a waveguide with planar boundaries is generated to be used as reference data outside a cylindrical inclusion. The domain is composed of an infinite strip confined in $\Omega_s = \{x_1 \in \mathbb{R},\ x_2 \in (-h, 0)\}$, featuring no energy radiation conditions at the lateral boundaries. The Helmholtz equation is again valid in $\Omega' = \Omega_s \setminus \bar{D}$, while the same boundary conditions are applied on the surface of the scatterer. Homogeneous Neumann boundary conditions are applied on both upper and bottom strip surfaces. Hence it holds,

$$\nabla^2\varphi + k^2\varphi = 0 \text{ in } \Omega' \tag{A6}$$

$$\alpha\frac{\partial\varphi}{\partial n} + \beta\varphi = -\left(\alpha\frac{\partial\Phi_I}{\partial n} + \beta\Phi_I\right) = g \text{ on } \Gamma_S \tag{A7}$$

$$\frac{\partial\varphi(x_1,0)}{\partial x_2}=\frac{\partial\varphi(x_1,-h)}{\partial x_2}=0. \tag{A8}$$

Finally outgoing solutions are assumed at the vertical end boundaries.

Analytical solutions corresponding to radiating field in homogeneous waveguides with planar boundaries, in the absence of inclusions, can be easily constructed by the method of multiple images (see Jensen et al., 2011, Brekhovskikh and Lysanov 2003). For simplicity, we consider the field emitted by an infinite series of $2m$ mirror sources positioned along the x_2 axis at h intervals, defined as follows

$$\varphi(x_1,x_2)=\sum_{m=-\infty}^{\infty}H_0^{(1)}(kr_m),\quad \text{with}\quad r_m=\sqrt{x_1^{\,2}+(x_2-mh)^2}. \tag{A9}$$

See Fig. A.3(a). The produced radiating wavefield satisfies the imposed homogeneous Neumann conditions on the waveguide planar boundaries. However, it is known that the series (A9) is slowly convergent, hence an alternative representation can be obtained by separation of variables in the form of a normal mode series (see Jensen et al., 2011) where the wavefield potential is given as a sum of eigenfunctions for the infinite strip Ω_s ,

$$\varphi(x_1,x_2)=2\sum_{n=0}^{\infty}\tilde{Y}_n(x_2)\tilde{Y}_n(x_{2s})\frac{\exp\left(ik_{x_1n}|x_1-x_{1s}|\right)}{k_{x_1n}}, \tag{A10}$$

with the horizontal and vertical wavenumbers given as $k_{x_1n}=\sqrt{k^2-k_{x_2n}^{\,2}}$ and $k_{x_2n}=n\pi/h$. The functions $\tilde{Y}_n(y)=Y_n(y)/\|Y_n\|$, represent the normalized vertical structure of the modes. The vertical modes corresponding to eigenvalues k_{x_2n} are chosen as $Y_n(y)=\cos\left(k_{yn}(y+h/2)\right)$ in order to satisfy the planar boundary conditions.

The latter series (A10) can be truncated, keeping the propagating and a number of evanescent modes sufficient for rapid convergence in the whole region outside a ball in the vicinity of the fictitious source, i.e. $kr_0>\varepsilon$. Indicative plots of the waveguide solution are shown in Fig.A.4 with imposed Neumann Conditions on the planar boundaries, for *ka* =1 and *kh* =12.

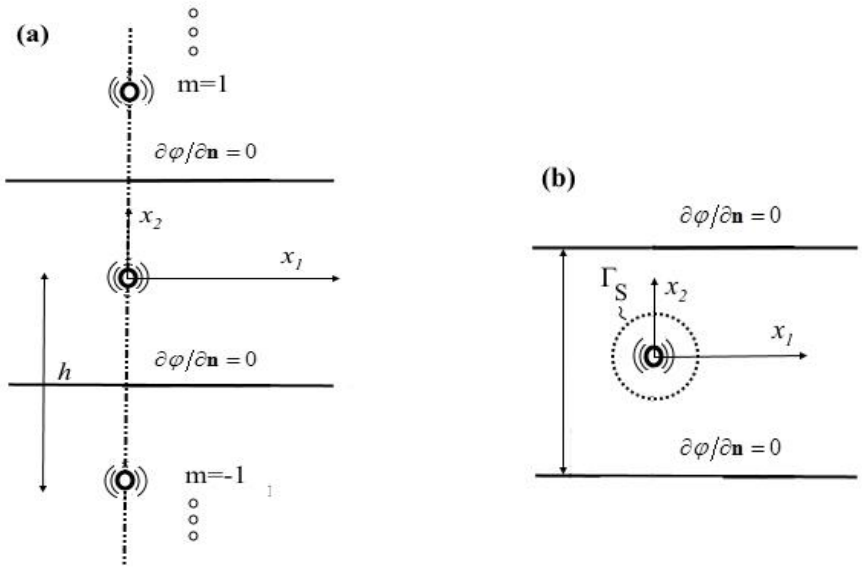

Figure A3 (a) Scattering in a simple waveguide in the absence of inclusions with the method of images (b) Scattering field in a simple waveguide with the method of images

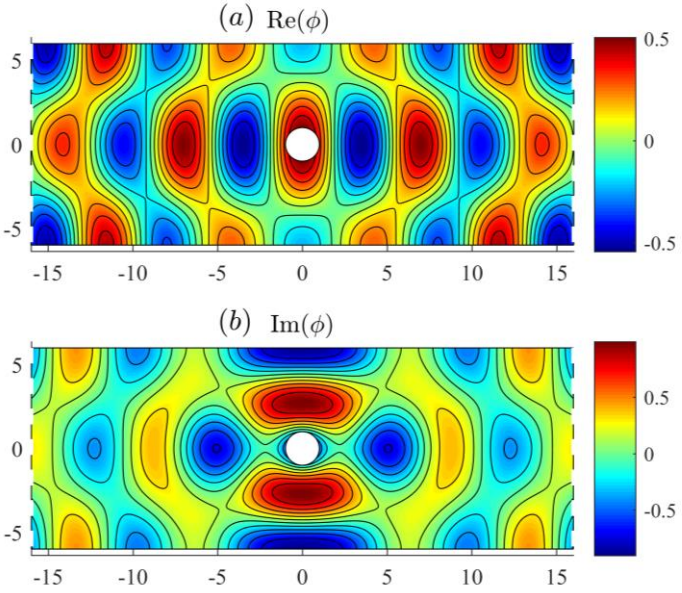

Figure A4. Solution in the examined simple waveguide with imposed Neumann Conditions on the planar boundaries, for *ka*=1 and *kh*=12 . (a) Real part, (b) Imaginary part.

Published in Ocean Engineering - Volume 179, 1 May 2019, Pages 307-324

References

Abarbanel, S., Gottlieb, D., 1997. A Mathematical Analysis of the PML Method, J. Comput. Phys. 134(2), 357-363.

Belibassakis, K., A., Athanassoulis, G., A., Gerostathis, Th., P., 2001. A coupled mode model for the refraction-diffraction of linear waves over steep three-dimensional bathymetry. App. Ocean Res. 23, 319-336.

Belibassakis, K., A., Athanassoulis, G.,A., Gerostathis, Th., 2014. Directional wave spectrum transformation in the presence of strong depth and current inhomogeneities by means of coupled-mode model. Ocean Eng. 87, 84–96.

Belibassakis, K., A., Athanassoulis, G.,A., Papathanassiou, T.,K., Filopoulos, S.,P., Markolefas, S., 2014. Acoustic wave propagation in inhomogeneous, layered waveguides based on modal expansions and hp-FEM, Wave Motion 51, 1021-1043.

Belibassakis, K.A., Gerostathis, Th., Athanassoulis, G.A., 2011. A coupled-mode model for water wave scattering by horizontal, non-homogeneous current in general bottom topography. Appl. Ocean Res. 33, 384– 397.

Berenger, J., P., 1994. A perfectly matched layer for the absorption of electromagnetic waves. J. Comput. Phys. 114, pp. 185-200.

Berkhoff, J., C., W, 1972. Computation of combined refraction-diffraction. In Proc. 13th Int. Conf. on Coastal Engineering, Vancouver.

Berkhoff, J.C.W., Booy, N., Radder, A.C., 1982. Verification of numerical wave propagation modeis for simple harmonic linear water waves. Coastal Eng. 6, 255-279.

Bermudez, A., Hervella-Nieto L., Prieto, A., Rodriguez, R., 2010. Perfectly matched layers for time-harmonic second order elliptic problems, Arch. Comput. Methods 17, 77-107.

Bermudez, A., Hervella-Nieto, L., Prieto, A., Rodriguez, R., 2007. An optimal perfectly matched layer with unbounded absorbing functions for time-harmonic acoustic scattering problems. J. Comput. Phys. 223(2), 469-488.

Booij, N., 1983. A note on the accuracy of the mild slope equation, Coast. Eng. J., 191-203.

Brekhovskikh, L., M., Lysanov, Y.P., 2003. Fundamentals of Ocean Acoustics. Springer-Verlag, New York..

Chai, Y., Li W., Gong, Z., Li ,T., 2016. Hybrid smoothed finite element method for two-dimensional underwater acoustic scattering problems. Ocean Eng. 116, 129–141.

Chamberlain, P., G., Porter, D., 1995. The modified mild slope equation. J. Fluid Mech. 291, 393-407.

Cimpeanu, R., Martinsson, A., Heil, M., 2015. A parameter-free perfectly matched layer formulation for the finite-element-based solution of the Helmholtz equation. J. Comput. Phys. 296. 329–347.

Collino, F., Monk, P., 1998a. Optimizing the perfectly matched layer, Comput. Methods in Appl. Mech. Eng. 164, 157-171.

Collino, F., Monk, P., 1998b. The Perfectly Matched Layer in Curvilinear Coordinates, J. Sci. Comp. 19 (6), 2061-2090.

Dingemans, M., 1997. Water wave propagation over uneven bottoms. World Scientific.

Givoli D., 1992. Numerical methods for problems in infinite domains, Elsevier Science Publishers, Netherlands.

Givoli, D., 1991. Non-reflecting boundary conditions, J. Comput. Phys., 94, pp. 1-29.

Givoli, D., 2004. Higher-order local non reflecting boundary conditions: a review, Wave Motion 39, 319-326.

Guo, X., Wang, B., Mei, C.,C., Liu, H., 2017. Scattering of periodic surface waves by pile-group supported platform, Ocean Eng. 146, 46–58

Harari. I.. Albocher, U., 2006. Studies of FE/PML for exterior problems of time-harmonic elastic waves, *Comp. Meth. Appl. Mechanics and Engineering* 195, 3854-3879.

Jensen, F., Kuperman, W., Porter, M., Schmidt, H., 2011. Computational Ocean Acoustics. Springer Verlag, New York,

Kirby, J., T., 1984. A note on linear surface wave current interaction over slowly varying topography, J. Geophys. Res. 89, 745-747.

Kirby, J., T., Dalrymple, R., A., 1986. An approximate model for nonlinear dispersion in monochromatic wave propagation models. Coastal Eng. 9, 545-561.

Lassas, M., Somersalo, E., 1998. On the existence and Convergence of the solution of PML equations. Computing 60, 229-241.

Liu, P., L., F., 1983. Wave-current interactions on a slowly varying topography. J. Geophys. Res. 88, 4421-4426.

Martin, P., A., 2005. Multiple Scattering: Interaction of time-harmonic waves with N obstacles. Cambridge University.

Massel, S., R., 1993. Extended refraction-diffraction equation for surface waves, *Coastal Eng.* 19, 97-127.

Mei, C.,C., 1994. The applied dynamics of ocean surface waves. World Scientific, Singapore.

Miles, J., W., Chamberlain, P.,G., 1998. Topographical scattering of gravity waves, J. Fluid Mech. 361, 175–188.

Modesto, D., Fernádez-Méndez, S., Huerta, A., 2016. Elliptic harbor wave model with Perfectly Matched Layer and exterior bathymetric effects. J Waterw. Port Coast. Ocean Eng. 142 (5).

Modesto, D., Zlotnik, S., Huerta, A., 2015. Proper generalised decomposition for parameterised Helmholtz problems in heterogeneous and unbounded domains: Application to harbour agitation. Comput. Methods Appl. Mech. Eng. 295, 127-149.

Navon, I., M., Neta, B., Hussainy, M.,Y., 2004. A perfectly matched layer approach to the linearised shallow water equations models, Mon. Weather Rev. 132, 1369-1378.

Oliveira, F., 2004. Assessment of open boundary conditions on the elliptic formulation of the mild slope equation, Ocean Eng. 31, 1567-1576.

Oliveira, F., S., B.,F., Anastasiou, K., 1998. An efficient computational model for water wave propagation in coastal regions. Appl. Ocean Res. 20, 263-271.

Oskooi, A., F., Zhang, L., Avniel, Y., Johnson, S. G., 2008. The failure of perfectly matched layers and towards their redemption by adiabatic absorbers. Opt. Express 16 (15), 11376-11392.

Panchang, V., G., Pease, B., R., Wei, G., Cushman-Roisin, B., 1991. Solution of the mild-slope wave problem by iteration. Appl. Ocean Res. 13(4), 187-199.

Qi, Q., Geers, Th., L., 1998. Evaluation of the Perfectly Matched Layer for Computational Acoustics. J. Comput. Phys. 139, 166-183.

Rabinovich, D., Givoli, D., Becache, E., 2010. Comparison of high-order absorbing boundary conditions and perfectly matched layers in the frequency domain. Int. J. Numer. Meth. Biomed. Eng. 26, 1351-1369.

Radder, A., C., 1979. On the parabolic equation method for water wave propagation, *J. Fluid Mech*., 95, 159-176.

Radder, A., C., Dingemans, M., W., 1985. Canonical Equations for almost periodic, weakly non-linear gravity waves, Wave Motion 7, 473-485.

Published in Ocean Engineering - Volume 179, 1 May 2019, Pages 307-324

Rappaport, C.,M., 1995. Perfectly Matched absorbing boundary conditions based on anisotropic lossy mapping of space, IEEE Microw. Guided Wave Lett. 5(3), 90 – 92.

Ruiz, P.,M., Ferri, F., Kofoed, J., P., 2017. Water-wave diffraction and radiation by multiple three-dimensional bodies over a mild-slope bottom, Ocean Eng. 143, 163–176

Singer, I., Yefet, A., 2004. A perfectly matched layer for the Helmholtz equation. J. Comput. Phys. 201, 439-465.

Turkel, E., Yefet, A., 1998. Absorbing PML boundary layers for wave-like equations, Appl. Mumer. Math. 27, 533-557.